
























Probing AGN Feedback in Dwarf Galaxies with Spatially Resolved NIR Coronal Lines from JWST

ARCHANA ARAVINDAN ^{1,2,3} THOMAS BOHN ⁴ GABRIELA CANALIZO ¹ SHOBITA SATYAPAL ⁵ VIVIAN U ⁶
WEIZHE LIU ⁷ WILLIAM MATZKO ⁵ SARA DOAN ⁵ MATTHEW MALKAN ⁸ LEE ARMUS ⁹ TOHRU NAGAO ⁴
TANIO DIAZ-SANTOS ¹⁰ ADITYA TOGI ¹¹ THOMAS S.Y. LAI ⁹ SEAN T. LINDEN ⁷ MARINA BIANCHIN ^{12,13}
YI QING SONG ¹⁴ LORETO BARCOS-MUÑOZ ¹⁵ AARON EVANS ¹⁶ HANAE INAMI ¹⁷ KIRSTEN LARSON ¹⁸
SABRINA STIERWALT ¹⁹ AND JASON SURACE ²⁰

¹Department of Physics and Astronomy, University of California, Riverside, 900 University Ave, Riverside CA 92521, USA

²Department of Astronomy, The University of Texas at Austin, Austin, TX 78712, USA

³Cosmic Frontier Center, The University of Texas at Austin, Austin, TX 78712, USA

⁴Ehime University, Bunkyo-cho 2-5, Matsuyama, Ehime 790-8577, Japan

⁵Department of Physics and Astronomy, George Mason University, MS3F3, 4400 University Drive, Fairfax, VA 22030, USA

⁶IPAC, California Institute of Technology, 1200 E. California Blvd., Pasadena, CA 91125, USA

⁷Steward Observatory, University of Arizona, 933 N. Cherry Ave, Tucson, AZ 85721, USA

⁸Division of Astronomy and Astrophysics, University of California, Los Angeles, CA 90095

⁹IPAC, MC 320-6, Caltech, 1200 E. California Blvd., Pasadena, CA 91125

¹⁰Institute of Astrophysics - FORTH, GR-70013 Vassilika Vouton, Greece

¹¹Department of Physics, Texas State University, 601 University Drive, San Marcos, TX 78666, USA

¹²Instituto de Astrofísica de Canarias, Calle Vía Láctea s/n, E-38205, La Laguna, Tenerife, Spain

¹³Departamento de Astrofísica, Universidad de La Laguna, E-38206, La Laguna, Tenerife, Spain

¹⁴European Southern Observatory, Joint ALMA Observatory, Alonso de Córdoba, 3107, Vitacura, Santiago, 763-0355, Chile

¹⁵North American ALMA Science Center, National Radio Astronomy Observatory, 520 Edgemont Road, Charlottesville, VA 22903

¹⁶Department of Astronomy, University of Virginia, 530 McCormick Road, Charlottesville, VA 22904 NRAO, 520 Edgemont Road, Charlottesville, VA, 22903

¹⁷Hiroshima University, 1-3-1 Kagamiyama, Higashi-Hiroshima City, Hiroshima, 739-8526, Japan

¹⁸Space Telescope Science Institute, Baltimore, MD 21218

¹⁹Occidental College, 1600 Campus Road, Los Angeles, CA, 90041

²⁰IPAC, MC 314-6, Caltech, 1200 E. California Blvd., Pasadena, CA 91125

ABSTRACT

We present the first spatially resolved investigation of near-infrared coronal lines in dwarf galaxies hosting active galactic nuclei (AGN), using JWST/NIRSpec integral field spectroscopy. Coronal lines (CLs), which are forbidden transitions from highly ionized species with ionization potentials up to 450 eV, act as sensitive tracers of the AGN ionizing continuum and feedback processes. Across four dwarf galaxies with ionized gas outflows traced by the optical [O III] lines, we report the detection of 16 unique species of near-infrared CLs. Line ratio diagnostics indicate that photoionization from the AGN dominates the excitation of CLs. We find that the coronal line region in dwarf galaxies, traced by the various CLs, extends up to 0.5 kpc, and can constitute up to 10% of their host galaxy size. Correlations between CL luminosities and [O III] ionized gas outflow properties are consistent with a scenario in which AGN-driven outflows likely facilitate the detection of CLs and contribute to their extent. Several CLs, including [Si VI], [Si VII], and [Mg VIII], exhibit a secondary broad component ($W_{80} > 300 \text{ km s}^{-1}$). If we interpret this spatially compact gas as part of an outflow, this would indicate that the outflowing gas includes a wide range of ionizations. The estimated energetics imply this highly ionized component is compact yet powerful enough to perturb gas in the central regions of the host dwarfs. These results indicate that AGN in low-mass galaxies may produce outflows capable of influencing their structure and evolution.

Keywords: Active galactic nuclei (16) — AGN host galaxies (2017); Dwarf galaxies (416); Near infrared astronomy (1093); Active galaxies (17); Galaxy evolution (594) Galaxy winds (626) ; Extragalactic astronomy (506); Galaxy kinematics (602)

1. INTRODUCTION

Over the past decade, a growing number of studies have revealed that active galactic nuclei (AGN) are not limited to massive galaxies, but also occur in dwarfs with stellar masses below $\sim 10^9 M_\odot$ (A. V. Filippenko & L. C. Ho 2003; A. E. Reines et al. 2013; E. C. Moran et al. 2014; I. V. Chilingarian et al. 2018; M. Mezcuca & H. Domínguez Sánchez 2020; S. Salehirad et al. 2022; R. Pucha et al. 2025). Their presence in such low-mass systems provides new constraints on black hole seed formation and the role of feedback in shallow gravitational potentials (K. Inayoshi et al. 2020; M. Volonteri et al. 2021; S. Koudmani et al. 2021, 2022; U. Chadayammuri et al. 2023). Traditionally, stellar feedback from supernovae and young stars has been regarded as the dominant regulator of star formation and gas loss in dwarfs, but recent observations show that AGN can also drive galaxy-wide outflows (S. J. Penny et al. 2018; C. M. Manzano-King et al. 2019; W. Liu et al. 2024; S. Salehirad et al. 2025; V. Rodríguez Morales et al. 2025). In some cases, the mass and kinetic energy outflow rates of AGN in dwarf galaxies are comparable to those in massive galaxies when scaled by AGN luminosity (C. M. Manzano-King et al. 2019; W. Liu et al. 2020), and AGN-driven winds have been shown to be faster and more energetic than stellar-driven outflows in hosts of similar mass and at similar redshifts (A. Aravindan et al. 2023).

Unlike stellar feedback, which mostly acts locally and is limited by the star formation rate, AGN can inject energy on galaxy-wide scales, often with outflow velocities that exceed the escape velocity of dwarfs (C. M. Manzano-King et al. 2019). Even short-lived AGN episodes may therefore have disproportionate effects compared to continuous stellar activity, regulating star formation, removing gas and metals, and enriching the circumgalactic medium. If AGN feedback proves effective at these mass scales, it would imply that black hole growth and galaxy evolution are coupled across the full mass spectrum, challenging the paradigm that stellar feedback dominates in dwarfs while AGN feedback shapes massive galaxies (J. Silk 2011). This raises a key question: can AGN feedback play an equally significant role in dwarf galaxy evolution as in their massive counterparts?

A major obstacle in answering this question lies in confirming that the observed outflows are indeed AGN-driven. Common tracers of ionized gas such as [O III]

$\lambda 5007$ can suffer contamination from stellar processes, making it challenging to distinguish between stellar- and AGN-powered winds in these low-mass systems. This necessitates the need for observational diagnostics that are both sensitive to AGN photoionization and largely immune to stellar contamination (J. M. Cann et al. 2019).

Coronal lines (CLs), which are forbidden transitions from highly ionized species with ionization potentials up to 450 eV, satisfy these requirements. Their excitation typically requires the hard radiation field from an accreting black hole. Although recent observations have detected CLs in stellar winds from massive stars (D. R. Law et al. 2024), the presence of highly ionized (>150 eV) and extended CLs are unlikely to be produced by stellar populations alone (S. Satyapal et al. 2021; C. T. Richardson et al. 2022). Thus, CLs provide a unique window into the otherwise unobservable ionizing continuum of Type-2 AGN, and have been used to constrain the spectral energy distribution of the central engine, estimate black hole masses (J. M. Cann et al. 2018; A. Prieto et al. 2022), and trace the most highly ionized phases of AGN-driven outflows (F. Müller-Sánchez et al. 2011; D. May et al. 2018; V. U et al. 2022; M. A. Fonseca-Faria et al. 2023; L. Armus et al. 2023; M. Bianchin et al. 2024). Their high ionization potentials ensure that the emission is free from contamination by stellar outflows. In massive galaxies, CLs have been observed to extend beyond the narrow-line region, often tracing interactions between AGN jets and the interstellar medium (A. Rodríguez-Ardila et al. 2006; J. Negus et al. 2021; W. Matzko et al. 2025). Because CLs likely trace only the AGN-powered, most highly ionized phases of outflows, they provide a direct probe of AGN feedback. This is particularly critical in dwarf galaxies, where the shallow potential wells make them more susceptible to the gas-clearing effects of even modest AGN-driven winds (J. Silk 2017).

Despite their potential to identify AGN and AGN-feedback in more massive galaxies, CLs in dwarf galaxies remain largely unexplored. Photoionization modeling predicts that intermediate-mass black holes (IMBHs) in dwarfs should produce stronger CL emission due to their harder ionizing spectral energy distribution (SED) (J. M. Cann et al. 2018). Yet, only a small number of dwarf galaxies have reported detections of CLs, both in the optical and near-infrared (T. Bohn et al. 2021; J. M.

Table 1. Target Details

Name	Short name	Redshift	$\log(M_*/M_\odot)$	$\log(M_{BH}/M_\odot)$	$\log[L(\text{AGN})]$ (erg s^{-1})	SFR ($M_\odot \text{ yr}^{-1}$)	$W_{80, [\text{O III}] \text{ broad}}$ (km s^{-1})
(1)	(2)	(3)	(4)	(5)	(6)	(7)	(8)
J084234.51+031930.7	J0842	0.0291	9.3	5.8 ± 0.5 (i)	43.1 ± 0.4	<0.3	500
J090613.75+561015.5	J0906	0.0467	9.4	5.4 ± 0.3 (ii)	43.7 ± 0.8	<0.3	980
J095418.16+471725.1	J0954	0.0329	9.1	5.0 ± 0.4 (ii)	43.9 ± 1.1	<0.3	730
J100935.66+265648.9	J1009	0.0145	8.8	5.1 ± 0.1 (iii)	43.0 ± 1.0	<0.1	210

NOTE—Columns (1): SDSS name of the target. (2): Short name used in this paper. (3): Redshift, as measured from a combination of stellar absorption features and $\text{Pa}\alpha$ $1.86 \mu\text{m}$. (4): Stellar mass from the NASA Sloan Atlas (M. R. Blanton et al. 2011) with an average error of 0.5 dex. (5): Black hole mass derived using broad line fits and Eddington luminosities from the following references: (i) C. M. Manzano-King et al. 2019, (ii) A. E. Reines et al. 2013; F. R. Marleau et al. 2017, (iii) E. C. Moran et al. 2014. We caution that the estimated masses are uncertain, by 0.5 dex or more. (6): Bolometric AGN luminosity based on extinction-corrected [O III] luminosity (W. Liu et al. 2020, 2024). (7): Upper limit on the star formation rate (SFR) based on the extinction-corrected [O II] $\lambda\lambda 3726, 3729$ from W. Liu et al. 2020, assuming that one-third of the [O II] emission is from the star formation activity, following L. C. Ho 2005. (8): Median W_{80} measurements of the broad, outflowing component in [O III] determined from KCWI data (W. Liu et al. 2020).

Cann et al. 2021; M. Molina et al. 2021; M. Reeve et al. 2023; A. Aravindan et al. 2024). Ground-based NIR spectroscopy of dwarfs hosting AGN-driven, ionized-gas outflows has revealed high-ionization CLs (T. Bohn et al. 2021), but their spatial extents, kinematics, and connection to AGN feedback remain poorly constrained.

In this paper, we use JWST/NIRSpec integral field spectroscopy to spatially map the coronal line region (CLR) in dwarf galaxies hosting AGN and to examine its relationship to AGN-driven outflows. Our resampled $0.05''$ pixel scale of NIRSpec allows us to resolve the inner structure of the CLR, probe the spatial extent of NIR CLs, including several transitions at wavelengths $> 2.4 \mu\text{m}$, which are difficult to access from the ground, and confirm the AGN origin of observed outflows. By directly linking CL emission to feedback processes, we provide new constraints on the physical conditions, energetics, and influence of AGN in the low-mass regime. The paper is organized as follows: in Section 2.2, we present our JWST observations and data reduction; Section 3 describes our analysis and spatial mapping techniques; Section 4 presents our CL detections and the ionizing source; Section 5 discusses the coronal line region and implications for AGN feedback in dwarf galaxies; and Section 6 summarizes our findings. Throughout, we assume a flat ΛCDM cosmology with $H_0 = 70 \text{ km s}^{-1} \text{ Mpc}^{-1}$, $\Omega_m = 0.3$, and $\Omega_\Lambda = 0.7$.

2. OBSERVATIONS AND DATA REDUCTION

2.1. Sample selection: Presence of ionized gas outflows

We began with 29 Baldwin–Phillips–Terlevich (BPT; J. A. Baldwin et al. 1981)-selected, spatially extended,

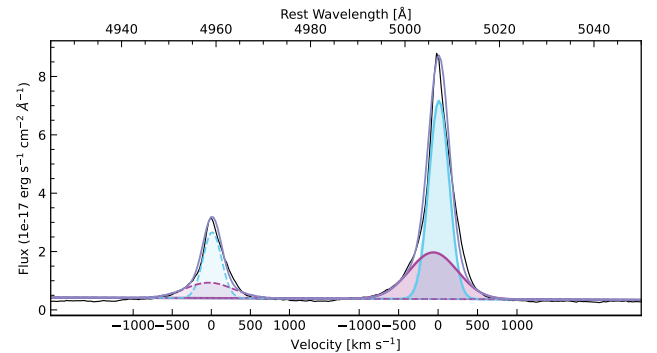


Figure 1. Keck/KCWI spectrum of J0906, one of the targets in the sample, showing the blue-shifted wings of [O III] within the central 0.5 kpc. All the targets observed with JWST exhibit similar ionized gas outflow profiles detected in [O III].

AGN-hosting dwarf galaxies (A. E. Reines et al. 2013; E. C. Moran et al. 2014; C. M. Manzano-King et al. 2019). Follow-up Keck/LRIS long-slit spectroscopy and Keck/KCWI IFU data isolated eight systems with galaxy-scale warm-ionized outflows traced by [O III] $\lambda\lambda 4959, 5007$ doublet (C. M. Manzano-King et al. 2019; W. Liu et al. 2020) (Figure 1). Near-IR spectroscopy with Keck/NIRES then detected CLs in five of these eight (T. Bohn et al. 2021). From this set, we selected four targets listed in Table 1 with stellar masses $< 10^{9.5} M_\odot$ for JWST/NIRSpec IFU that sample a range in stellar mass. Further details of the JWST sample will be provided in T. Bohn et al. 2025, in prep.

The [O III] emission profile in these galaxies has a broad, often blueshifted wing. C. M. Manzano-King

et al. 2019; W. Liu et al. 2020) model this with an additional Gaussian distinct from the narrow systemic gas with median bulk velocities of $\sim 240 \text{ km s}^{-1}$ and W_{80} up to $\sim 1200 \text{ km s}^{-1}$. HST/COS observations of three of the fastest systems (W. Liu et al. 2024) show definite outflows, producing blueshifted UV absorption in the C II, C IV, Si II, and Si IV lines. Photoionization modeling for one of the galaxies, J0954, places the absorbing gas at $\sim 0.5 \text{ kpc}$, suggesting a galactic-scale impact. The measured kinetic-energy outflow rates also exceed those of starburst winds at comparable SFRs (W. Liu et al. 2024). Keck/NIRES detections of [Si VI] (and other NIR CLs) often show higher outflow velocities than [O III], and the lack of J-band CN absorption features argues against a dominant young-stellar origin (T. Bohn et al. 2021). The lack of [O III] $\lambda 4363$ detection makes it challenging to estimate direct gas-phase metallicities for the observed targets. However, since BPT-selected AGNs in dwarf galaxies are expected to be biased toward higher metallicities (A. E. Reines et al. 2013), we assume that the metallicities are nearly solar.

2.2. JWST/NIRSpec Observations and Data Reduction

The data were obtained from the JWST Cycle 2 program (PID 3663, P.I.: Thomas Bohn). All four targets were observed with NIRSpec IFS (P. Jakobsen et al. 2022; T. Böker et al. 2023). J0906 was observed on 17 March 2024, J1009 on 9 May 2024, J0954 on 8 March 2024 and J0842 on 7 April 2024. Data were collected using the NIRSpec IFU high resolution mode in the G140H/F100LP, G235H/F170LP, and G395H/F290LP grating/filter combinations. The resulting wavelength coverage obtained with our choice of grating/filter combination was $0.9 - 5.2 \mu\text{m}$ with a nominal resolving power of $R \sim 2700$ (110 km s^{-1}). We obtained dedicated background observations for the four targets instead of the standard LeakCal exposures in order to subtract the background to detect any faint CL.

We downloaded the raw data files from the Barbara Mikulski Archive for Space Telescopes (MAST) and subsequently processed them with the JWST Science Calibration pipeline version 1.15.1 (H. Bushouse et al. 2023) under the Calibration Reference Data System (CRDS) context `jwst.1253.pmap`. The level 1 files downloaded from MAST were processed using the Detector1 stage (stage 1), which performs detector-level corrections and generates count-rate images. In order to remove artifacts generated by cosmic-ray hits on the detector, we applied the snowball flagging for the jump step during the first stage of the pipeline. We used the dedicated background exposures to perform the pixel-to-pixel background subtraction for each target in stage 2.

The stage2 images were then resampled and combined into a final data cube through the `Calwebb_spec3` processing (stage3) using the ‘drizzle’ method with a spaxel size of $0.05''$ to enhance the spatial resolution. The resulting data cubes display the well-known sinusoidal modulations in the spectrum caused by the limitation of the pipeline to correctly trace the target across the IFU slices during the rectification process. To correct these artifacts, also known as “wiggles”, we applied a custom code similar to that developed by M. Perna et al. 2023 that masks out the detected lines and models and subtracts the sinusoidal variations (see W. Matzko et al. 2025, in prep). After completing the pipeline reduction, we removed any remaining pixel outliers from the data cubes using the methods outlined in T. A. Hutchison et al. 2024.

3. ANALYSIS

3.1. Emission line fitting and spatial maps generation

To fit the various coronal emission lines (Table 2) and generate spatial flux and velocity maps, we used the Bayesian AGN Decomposition Analysis for Sloan Digital Sky Survey (SDSS) Spectra (BADASS v10.2.0, R. O. Sexton et al. 2021)¹ code. Through Markov Chain Monte Carlo routines, BADASS performs simultaneous multicomponent fits to emission-line spectra. Individual spaxels in the NIRSpec cubes were fit iteratively across the full spatial extent of the data cubes, where a third-order Legendre polynomial was used for the continuum. The host galaxy and the stellar line-of-sight velocity distribution were fit using the penalized pixel fitting method (pPXF, M. Cappellari & E. Emsellem 2004) with templates from the eMILES (A. Vazdekis et al. 2016) stellar library. Emission lines were modeled using Gaussian profiles. A secondary Gaussian component to the fit was included based on the line-testing option that is implemented within BADASS. We used a combination of multiple line testing options such as CHI2_RATIO and a modified F-test. The CHI2_RATIO test is the ratio of the reduced chi-squared values for each fitted model, and can be interpreted as the fraction of the difference in the residuals weighted by the noise. The modified F-test generates a confidence between 0 and 1 of the Monte-Carlo resampled maximum likelihood values of the simple and complex models. If the confidence is 0.9, the difference between residuals is significant, and an additional component is justified with 90% confidence. If the value of the CHI2_RATIO was > 0.1 and if the modified F-test confidence param-

¹ <https://github.com/remingtonsexton/BADASS3>

ter was > 0.9 , then adding a second component provided a significant improvement to the fit and was thus justifiable. This secondary component was restricted to have a larger velocity offset from the rest-frame wavelength (see Table 2) and a larger dispersion than the primary component (See Figure 2 for an example fit to a single spaxel and also Section 3.3). Due to the diverse emission profiles in our data, we left the amplitude and width as unrestricted free parameters for the primary component. We also set a signal-to-noise ratio (S/N) threshold of three for all lines and components within each spaxel to determine a detection. Uncertainties were derived from the error spectrum and the random errors associated with the Bayesian fitting process.

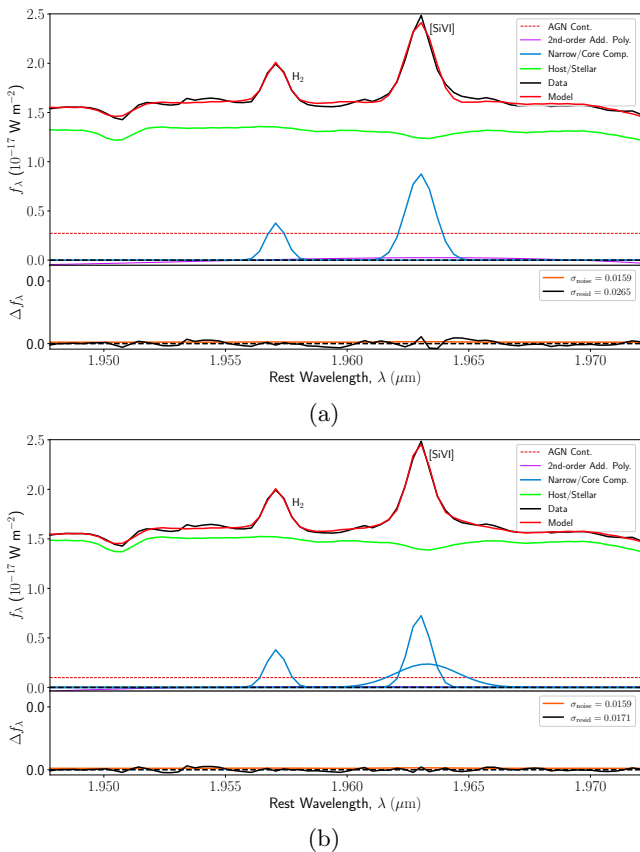


Figure 2. Examples of (a) one Gaussian component and (b) two Gaussian components fit to the [Si VI] line profile for J0954 for the same single spaxel. In each panel, the black spectrum is the observed data, the solid red line is the best fit, and the blue lines represent the Gaussian components. The residuals after subtraction from the best fit are shown at the bottom of each panel. We see that the single component in (a) does not adequately fit the observed line profile; based on the F-test and CHI2RATIO test, a second component is justified. A similar second component was also required in the central spaxels of [Si VII], [Si IX], [Mg IV], [Mg VIII] and [Ar VI] lines in J0954 and J1009.

3.2. Flux, v_{off} and W_{80} maps

Maps of the narrow component for a sample of CLs detected in our sample can be seen in Figure 3. The v_{off} shows the offset velocity (calculated from the best-fit Gaussian) from the expected central wavelengths from the systemic redshift (calculated from a combination of stellar absorption features and the strong Paschen α $\lambda 1.873 \mu\text{m}$ line) of the associated CL. The central wavelengths of each line were determined from the wavelengths compiled by CLOUDY². W_{80} is the line width defined to encompass 80% of the total flux, such that $W_{80} = v_{90} - v_{10}$, where v_{10} and v_{90} are the velocities at the 10th and 90th percentiles of the total flux, respectively, calculated starting from zero intensity on the red side of the line. For a Gaussian, W_{80} is 1.0833 times the Full Width at Half Maximum (FWHM). Thus, W_{80} can be used as an indicator of turbulent or disturbed gas in the galaxy or as the distribution of gas velocities in an outflow (G. Liu et al. 2013; A. Concas et al. 2017; S. Veilleux et al. 2020; J. Scholtz et al. 2021). All reported W_{80} values have been corrected for instrumental broadening. The flux maps indicate that most of the emission arises from a compact source at the center of each target. While several previous studies have suggested preferentially blue-shifted emission line profiles for CLs (J. M. Gelbord et al. 2009; M. Molina et al. 2021), we do not observe such a systematic preference. On the contrary, there seems to be a variety of observed v_{off} within the CL, ranging from blue-shifted to red-shifted values.

3.3. Presence of a broad component

Two of the targets (J0954 and J1009) have a significant number (≥ 4) of CLs that show signs of having broader wings than a single Gaussian (Figures 2 and 4), as determined by the line-component testing for the spectra in the individual spaxels (Section 3.1). Previous works have indicated that the optical coronal emission line profiles can be fitted by two-Gaussian components (M. A. Prieto et al. 2005; A. Rodríguez-Ardila et al. 2006; F. Müller-Sánchez et al. 2011). These studies also find that the first component extends to large distances (0.7 - 3.8 kpc). The second broader, weaker component cannot be measured outside of the bright nucleus (< 0.03 kpc). We find a similar trend in the two dwarf galaxies where broad CLs are detected (J0954 and J1009). We also find that the broad component is detected only in the stronger lines of [Si VI], [Si VII], [Mg IV], [Mg VIII], and [Ar VI]. The broad component is too weak to detect in weaker lines, including those with larger I.P. as well

² <https://linelist.pa.uky.edu/atomic/>

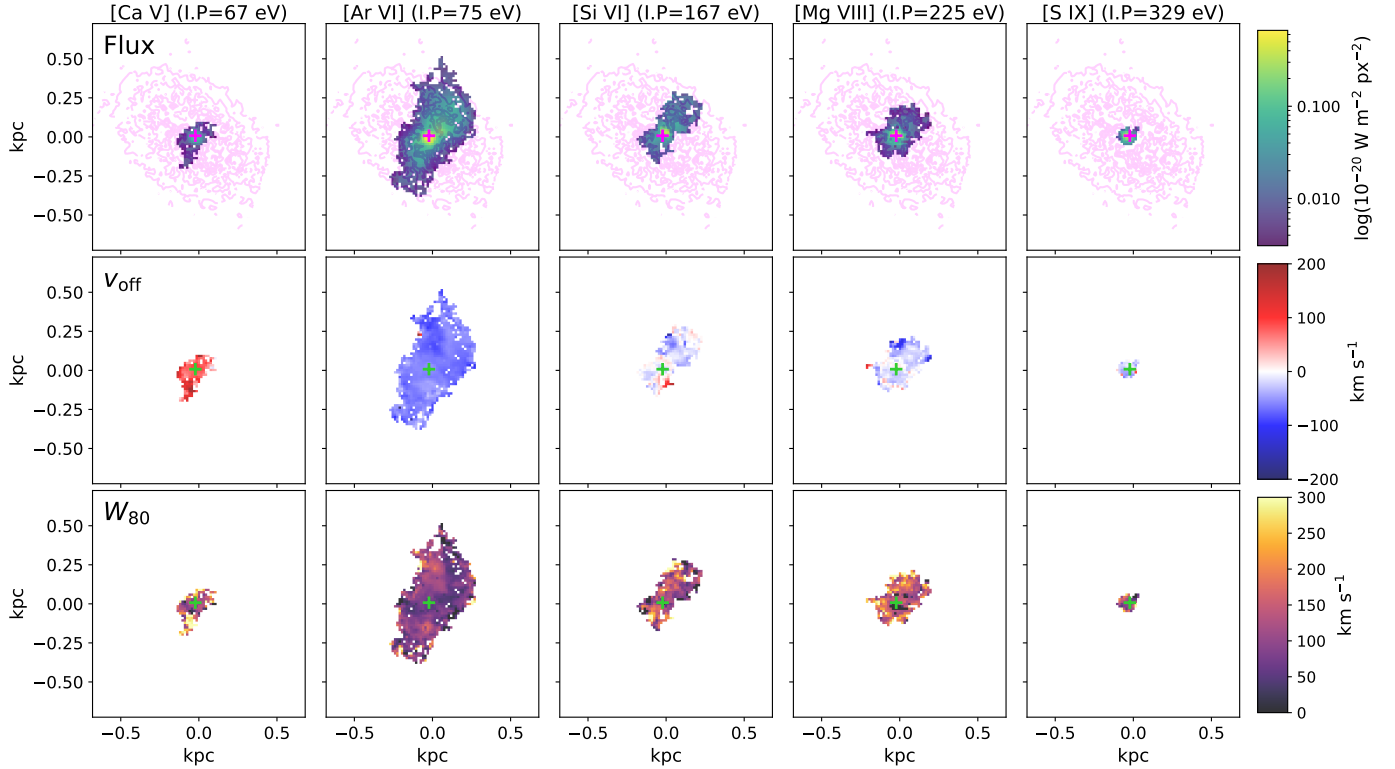


Figure 3. Flux, v_{off} and W_{80} maps of the narrow component for select CLs in J1009, in order of increasing I.P. The axes represent the physical scale in kpc. The magenta contours indicate the galaxy continuum, and we find that the CLs tend to be oriented perpendicular to the major axis of the galaxy continuum. The magenta and green crosses indicate the peak of the continuum flux and the potential AGN location (the slight (~ 1 pixel) mismatch in the peak can be attributed to PSF wandering between the different NIRSspec filters). The maps are oriented with North pointing up and East to the left.

as in Ca and Al lines which have similar I.P. as the aforementioned lines. The second component in all targets is significantly broad ($W_{80} > 300 \text{ km s}^{-1}$), but does not have significant velocity offset. For one of the targets (J0906), a second component was not included based on the line tests, but we find that the narrow component is significantly broad ($W_{80} > 300 \text{ km s}^{-1}$).

The presence of continuum “wiggles” (Section 2.2) in the data significantly limits the detailed characterization of the broad component. This posed challenges in fitting and getting resolved maps of the broad component. To fit the individual spaxels, we had to model the wiggles and remove them from the data. We found that it was impossible to distinguish between the wiggles and the faint wings of the outflows. To quantify the difference between the wiggled and de-wiggled cubes, we extract and fit spatially integrated spectra from each cube using the same aperture. We find that the parameter that was most affected by the uncertainty introduced by the wiggles is the width of the broad component, whereas fluxes and velocity offsets do not change significantly. We find that the width parameters, such as W_{80} and FWHM of the broad components, were lower by 20-30% in the de-wiggled cube as compared to the wiggled cubes. Thus

all the estimates of the W_{80} of the broad component in this work should be treated as lower limits.

3.4. Determining the extent of the CLs

To measure the spatial extent of each NIR CL, we first identify the central position $(x_{\text{center}}, y_{\text{center}})$ as the pixel with the peak flux. We then locate the furthest spaxel $(x_{\text{ext}}, y_{\text{ext}})$ from the center with a S/N of at least 3. To account for projection effects, we de-project this distance using the galaxy inclination angle i , estimated from the ratio of the semi-minor axis to the semi-major axis, b/a . We compute $\cos i = b/a$, where b/a is the exponential fit b/a value (`expAB_r`) obtained from the SDSS `PhotObj` catalog.

The de-projected extent in spaxel units is calculated using Equation (1) from J. Negus et al. 2021:

$$\text{Extent} = \sqrt{(x_{\text{ext}} - x_{\text{center}})^2 + [(y_{\text{ext}} - y_{\text{center}}) \cdot \cos i]^2} \quad (1)$$

We then convert the extent to physical units (kpc) using the `astropy.cosmology` Python package. We also estimate the extent using alternative definitions, including the half-light radius, 95th-percentile radius (R_{95}) and root-mean-square (rms) radius, and find that the

[Si VI], 1.963 μm , I.P.=167.0 eV

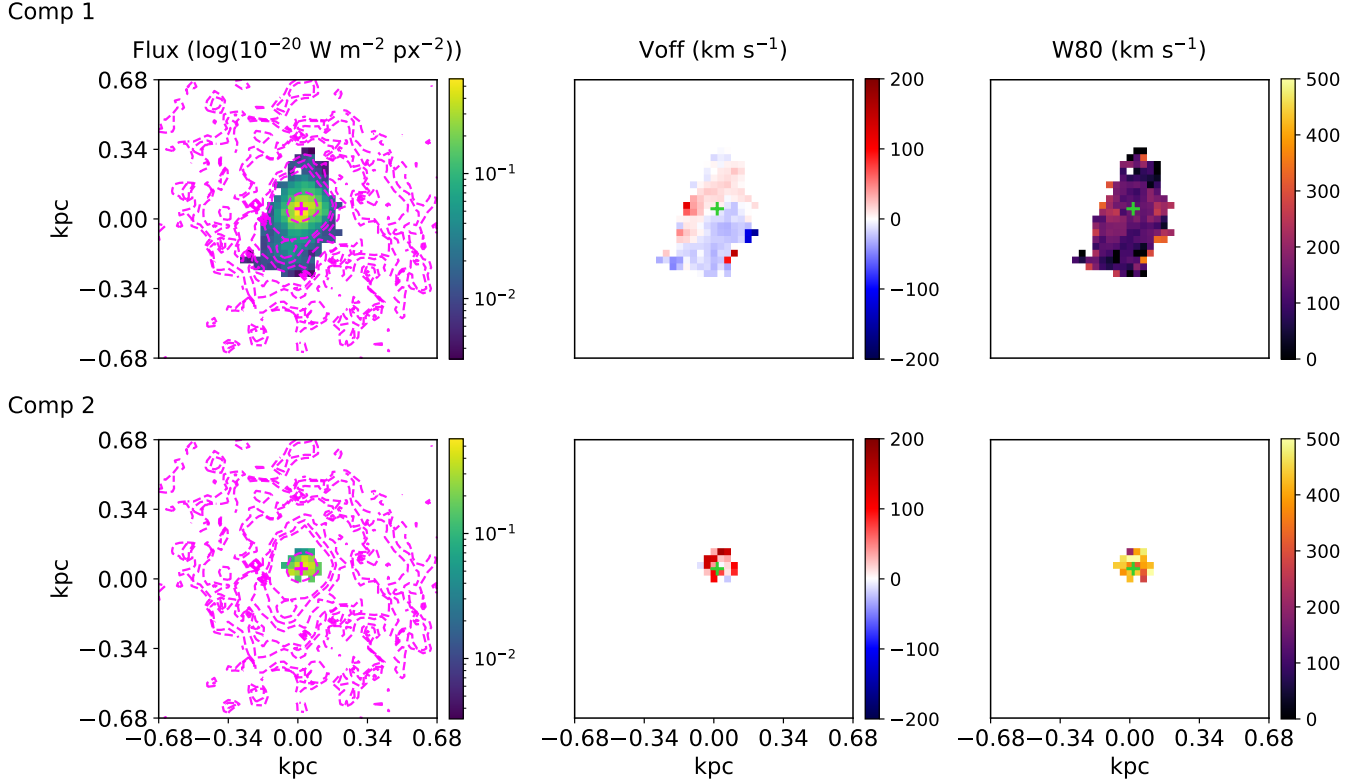


Figure 4. Flux, v_{off} and W_{80} maps, showing the two components in the [Si VI] line in J0954. The magenta contours trace the galaxy continuum and the cross indicates the peak continuum flux corresponding to the AGN position. The detected second component (bottom panel) across all the lines is found to be more compact than the first component, is concentrated in the central region and has larger W_{80} values than the first component.

trends described in Section 5.2 remain valid across these methods.

We then checked whether the CL extents are set by the line strength. First, we varied the S/N threshold from 1.5 to 3σ and required the inferred extent to change by $\leq 15\%$. For non-detections, we computed a 3σ PSF-aperture flux limit ($\sigma = F/(S/N)$) and compared it to the flux predicted from a reference line of the same element ([Si VII] for Si, [Mg VIII] for Mg, [S VIII] for S, and [Ca V] for Ca) assuming lines from the same species share a common spatial profile. For elements lacking multiple ionization stages (e.g., [Al VI], [Na VII]), we compared to the brightest available CL, [Ar VI]. We classified a line as absent only when the predicted flux exceeds the 3σ limit. Thus, the reported extents trace real emission boundaries rather than sensitivity limits or single-pixel artifacts, within the stated uncertainties.

4. RESULTS

4.1. Coronal line detections

Previous ground based NIR observations using Keck/NIRES (T. Bohn et al. 2021) revealed the presence of high-ionization CLs in the four targets between 0.9 - 2.3 μm . We now report the detection of new CLs due to the improved sensitivity as well as in the extended wavelength range provided by JWST/NIRSpec (0.9 - 5 μm). T. Bohn et al. 2021 reported a single CL, [Ca VIII], in J0842, which we do not detect in our JWST/NIRSpec observations. However, the expected wavelength of [Ca VIII] lies very close to the detector gap in the data cube, which makes it challenging to detect robustly. We also detect [Mg IV] at 4.48 μm , which is the only coronal line reliably observed in this target with NIRSpec. For J0906, T. Bohn et al. 2021 identified five CLs from ground-based data. We recover four of these in the NIRSpec spectra. [Ca VIII] is not detected as it falls within the transmission gap between the two

Table 2. Summary of Coronal Line (CL) Emission in the Targets

CL	λ (μm)	I.P. (eV)	$\log n_{\text{crit}}$ (cm^{-3})	J0842	J0906	J0954	J1009
	(μm)	(eV)	(cm^{-3})				
(1)	(2)	(3)	(4)	(5)	(6)	(7)	(8)
[S VIII]	0.9911	281	9.47	...	\checkmark^\dagger	\checkmark^\dagger	\checkmark^\dagger
[S IX]	1.2520	329	9.42	...	\checkmark^\dagger	\checkmark^\dagger	\checkmark^\dagger
[Si X]	1.4301	351	6.70	...	\checkmark^\dagger	\checkmark	...
[S XI]	1.9220	447	7.98	...	\checkmark^*	...	\checkmark
[Si VI]	1.9630	167	8.72	...	\checkmark^\dagger	\checkmark^\dagger	\checkmark^\dagger
(Broad)				\checkmark	\checkmark
[Ca VIII]	2.3205	127	6.66	\dagger	\dagger	\checkmark^*	\checkmark^\dagger
[Si VII]	2.4826	205	8.48	...	\checkmark	\checkmark	\checkmark
(Broad)				\checkmark	\checkmark
[Si IX]	2.5839	304	8.04	\checkmark	\checkmark
[Mg VIII]	3.0276	225	6.84	...	\checkmark	\checkmark	\checkmark
(Broad)				\checkmark	\checkmark
[Ca IV]	3.2061	51	7.10	...	\checkmark^*	\checkmark	\checkmark
[Al VI]	3.6593	154	5.88	\checkmark	\checkmark
[Si IX]	3.9357 [#]	304	8.04	\checkmark
(Broad)				\checkmark
[Ca VII]	4.0864	109	7.28	\checkmark	\checkmark
[Ca V]	4.1574	67	6.53	...	\checkmark^*	\checkmark	\checkmark
[Mg IV]	4.4871	80	7.24	\checkmark	\checkmark^*	\checkmark	\checkmark
(Broad)				\checkmark
[Ar VI]	4.5280	75	7.33	...	\checkmark^*	\checkmark	\checkmark
(Broad)				\checkmark	\checkmark
[Na VII]	4.6834	172	6.66	\checkmark

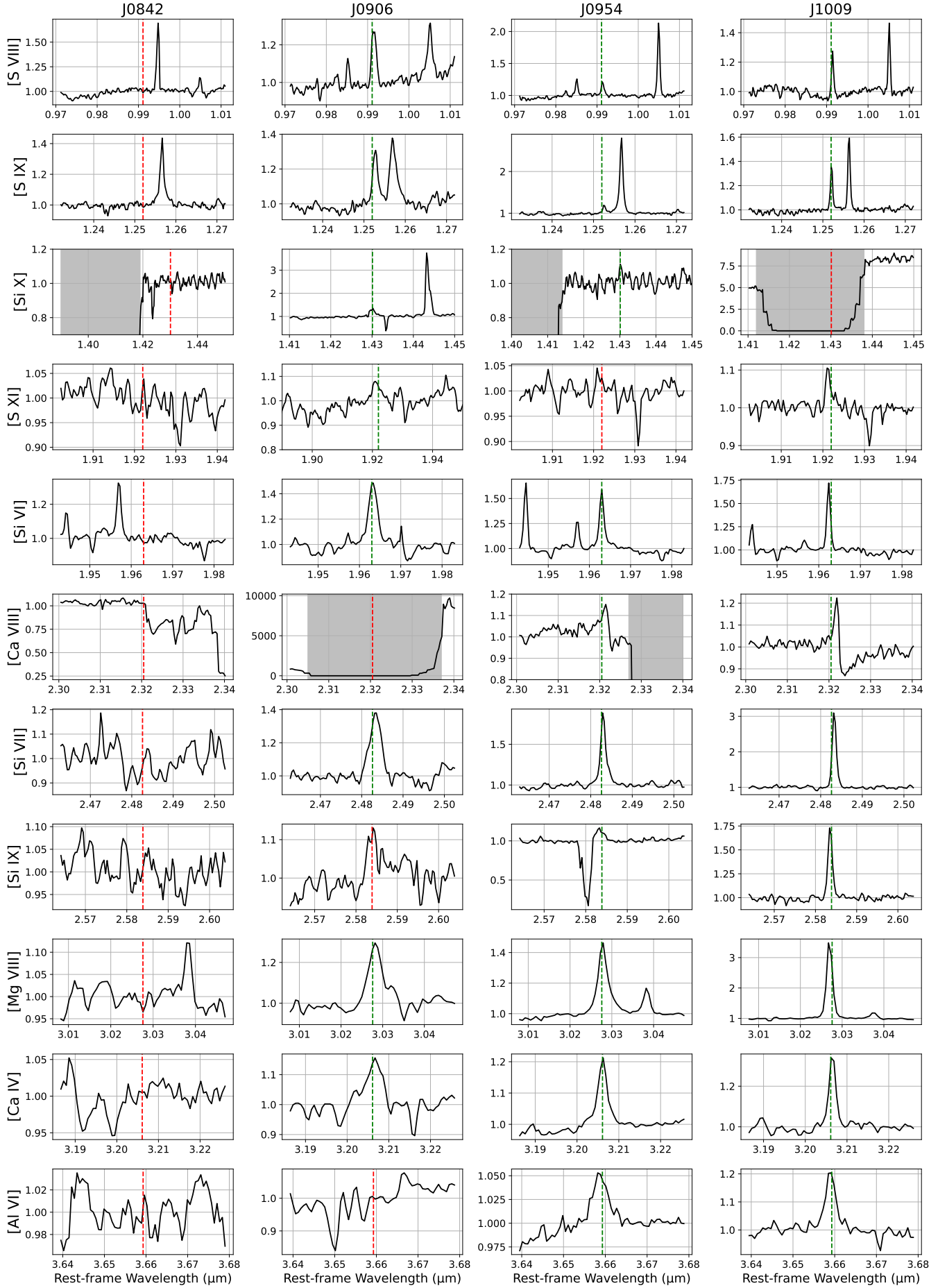
NOTE— Columns: (1) Coronal line species; (2) Rest wavelength from CLOUDY (μm). [#] indicates wavelength from the CAFE (T. Diaz-Santos et al. 2025) linelist^a. (3) Ionization potential (eV) from the Chianti database^b. (4) Critical density ($\log \text{cm}^{-3}$) from CLOUDY. (5–8) Detection status in each galaxy: \checkmark = detected with JWST/NIRSpec; \checkmark = broad component detected; \dagger = previously detected with Keck/NIRES; * = detected only in the 0.3'' integrated spectrum (not across individual spaxels).

^a<https://github.com/GOALS-survey/CAFE>

^b<https://www.chiantidatabase.org>

NIRSpec detectors. In addition to the previously known lines, we detect six new CLs, increasing the total number of NIR-detected CLs in this galaxy to 11. In J0954, three NIR CLs had been previously reported (T. Bohn et al. 2021). Our observations reveal 11 additional CLs, bringing the total to 14. Finally, J1009 exhibits the richest coronal line spectrum among the four targets. While previous ground-based observations identified four CLs, our NIRSpec data reveal 12 additional lines. These include several highly ionized species such as [S XI] (I.P. = 447 eV), as well as multiple ionization states of Ca and Na. For a complete list of detected CLs in the four targets see Tab. 2 and Figure 4.

Overall, we detect all CLs reported by T. Bohn et al. 2021 except those that fall in the JWST detector gap. We do not confirm the [Ca VIII] detection reported by T. Bohn et al. 2021; given its 2.2σ significance, it may have been a noise artifact. Among the new lines, only one ([S XI]) lies within the Keck/NIRES wavelength range but was likely missed due to lower sensitivity or imperfect atmospheric subtraction. [Si X] was not detected with Keck/NIRES in J0954 but is seen with NIRSpec, likely due to the higher spectral resolution. The remaining new detections are enabled by the extended wavelength coverage of NIRSpec.



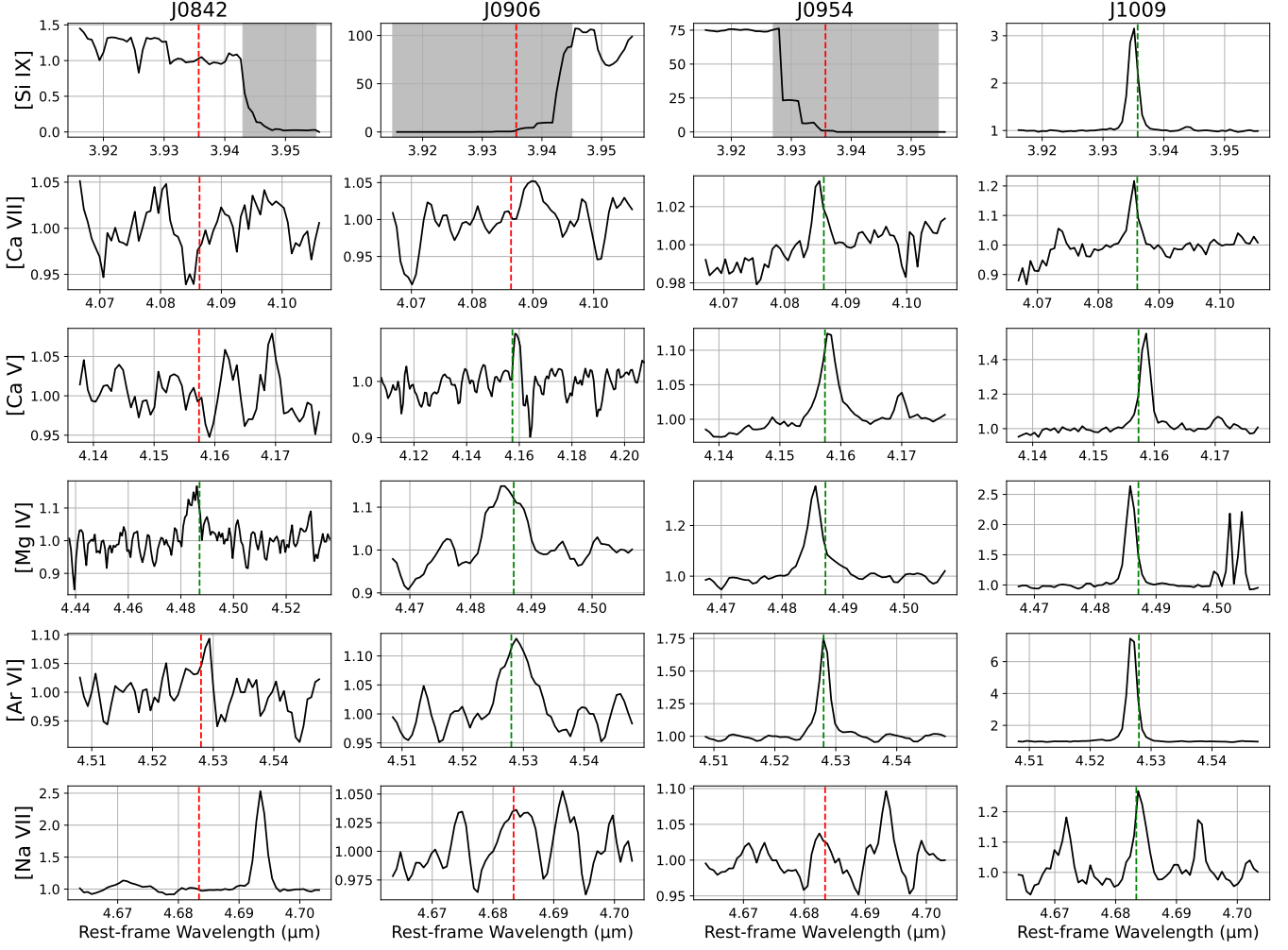


Figure 4. Zoomed-in spectra taken from a $0.3''$ radius aperture centered on the galaxy nucleus showing the detected ($>3\sigma$; green dotted lines) CLs in the four targets. The non-detections are indicated by the red dotted lines. Although in certain panels, there may be features that are indicative of CL lines, we only claim a detection if the line is $>3\sigma$ above the noise. The continuum flux is normalized to unity and the systemic redshift was used to shift the spectra to rest-frame wavelength. The JWST/NIRSpec detector gaps are indicated by the gray shaded region.

Three of the four targets also show optical CLs in prior SDSS, Keck/LRIS, Keck/KCWI and Gemini/GMOS spectra (C. M. Manzano-King et al. 2019; T. Bohn et al. 2021). J0906 has [Ne V] $\lambda 3426$, [Fe X] $\lambda 6374$ and [Fe VII] $\lambda\lambda 5721, 5159, 6087$. J0954 has [Ne V] $\lambda\lambda 3346, 3426$, [Fe V] $\lambda 3839$, and [Fe VII] $\lambda\lambda 5159, 6087$. J1009 has possible detections of [Fe VII] $\lambda\lambda 5721, 6087$. J0842 has no previously detected optical CLs.

The CL peaks in all targets coincide with the K-band continuum peak, and, within each target, the CL peaks coincide with one another, strongly suggesting that they are produced by the central AGN source. Although CLs have also been attributed to tidal disruption events (TDEs; J. T. Hinkle et al. 2023; P. Clark et al. 2024), a comparison between the JWST spectra and Keck/NIRES observations taken ~ 5 years earlier

(T. Bohn et al. 2021) shows no evidence of fading of the CLs. A five-year interval is consistent with the expected fading timescales of TDE-driven CLs (C.-W. Yang et al. 2013). Thus, it is unlikely that these CLs are produced by a TDE and are instead directly ionized by the central AGN.

4.2. Source of Ionization

While high-ionization CLs are generally attributed to photoionization by the hard radiation field of the AGN, some studies have proposed that they may also be produced by fast radiative shocks associated with outflows (M. A. Dopita & R. S. Sutherland 1995). Given that the dwarf galaxies in our sample exhibit evidence of outflows, we investigate the dominant ionization mechanism responsible for the observed CLs.

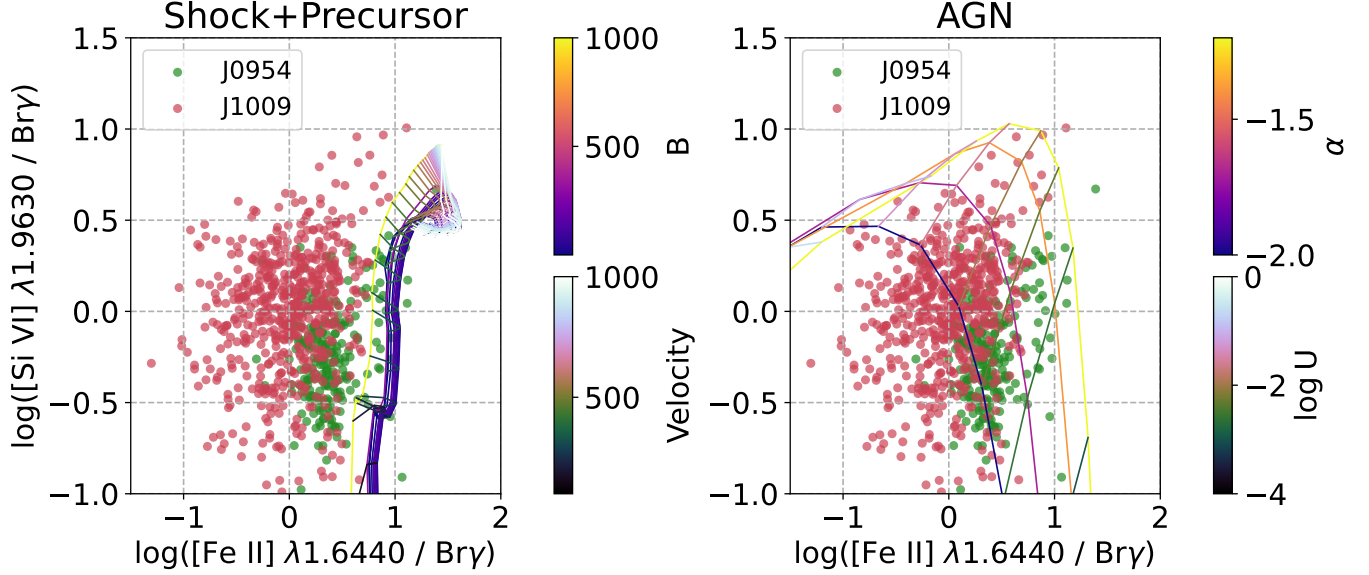


Figure 5. Shock+Precursor model (left) and AGN models (right) for [Si VI] for J0954 (green) and J1009 (red). The free parameters for the Shock+Precursor model (left) are B and velocity, where B is the transverse magnetic field strength in μG , velocity is the shock velocity in km s^{-1} . The free parameters for the AGN model (right) are α , which is the power-law index indicating the steepness of the power-law slope and $\log U$, which is the ionization parameter. The points represent values from individual spaxels wherever all the four lines used in the ratios were detected. We find that the observed line ratios largely agree with the AGN photoionization model for these two targets.

To disentangle the contributions from AGN photoionization and shocks, we utilize diagnostic flux ratios such as $[\text{Si VI}]/\text{Br}\gamma$ and $[\text{Si VII}]/\text{Br}\gamma$ vs. $[\text{Fe II}] 1.64 \mu\text{m}/\text{Br}\gamma$. The $[\text{Fe II}]$ line is a well-established tracer of shock excitation (V. U et al. 2013), whereas $\text{Br}\gamma$ traces star formation and the overall ionizing photon field. These ratios are compared against both AGN photoionization models from B. A. Groves et al. 2004a,b and shock+precursor models from M. G. Allen et al. 2008, as implemented in the IDL Tool for Emission-line Ratio Analysis (ITERA; B. A. Groves & M. G. Allen 2010). We plot the ratios obtained from the total fluxes of the emission lines from individual spaxels in two of the galaxies (J0954 and J1009), where all the lines are present in Figure 5.

The shock models account for both the shocked gas and the photoionized precursor region ahead of the shock front. The free parameters include the shock velocity ($v_{\text{shock}} = 10\text{--}1000 \text{ km s}^{-1}$) and the magnetic parameter $B/n^{1/2}$ (ranging from 10^{-4} to $10, \mu\text{G cm}^{3/2}$), where B is the transverse magnetic field strength. The AGN models assume a power-law ionizing spectrum ($F_{\nu} \propto \nu^{\alpha}$) with $5 \text{ eV} < \nu < 1000 \text{ eV}$, with a range of possible slopes α , and a range of ionization parameters $U = n_{\text{ion}}/n_e$, where n_{ion} is the ionizing photon density and n_e is the electron density.

As shown in Figure 5, most of the spatially resolved emission-line ratios for J0954 and J1009 align more closely with the AGN photoionization models.

Within the AGN photoionization grids, the points scatter around the gridline with more negative α , indicating a steeper power-law spectrum, which can be linked to factors like higher accretion rates and potentially lower black hole masses (E. Piconcelli et al. 2005; W. Ishibashi & T. J. L. Courvoisier 2010). The results are still valid when we use other CLs (i.e. $[\text{Si VII}]$). We assume solar metallicity for the grids, similar to W. Liu et al. 2020 and T. Bohn et al. 2021, but we find that if we assume lower metallicities for these dwarf galaxies (W. Cai et al. 2020), the results are still broadly valid. There is an upward shift of the spaxels towards the shock+precursor grids as well as towards higher α and $\log U$ values in the AGN grids for lower metallicities, but this shift is 0.1 dex for $0.5Z_{\odot}$ and 0.2 dex for $0.25Z_{\odot}$.

We further examine how the line ratios change with radial distance from the nucleus for the two targets. In J1009, we do not see any clear trend between the radius and the line ratios. However, for J0954, we find that near the galaxy center the ratios are consistent with pure AGN photoionization. At larger radii, they shift slightly towards values predicted by the shock+precursor models (Figure 6). However, this shift is not strong enough to require a significant contribution from shocks, as the ratios also remain broadly consistent with the photoionization models. Furthermore, since the CL emission follows the AGN ionization bicone (see Section 5.3), declines with radius, and does not show excess emission at

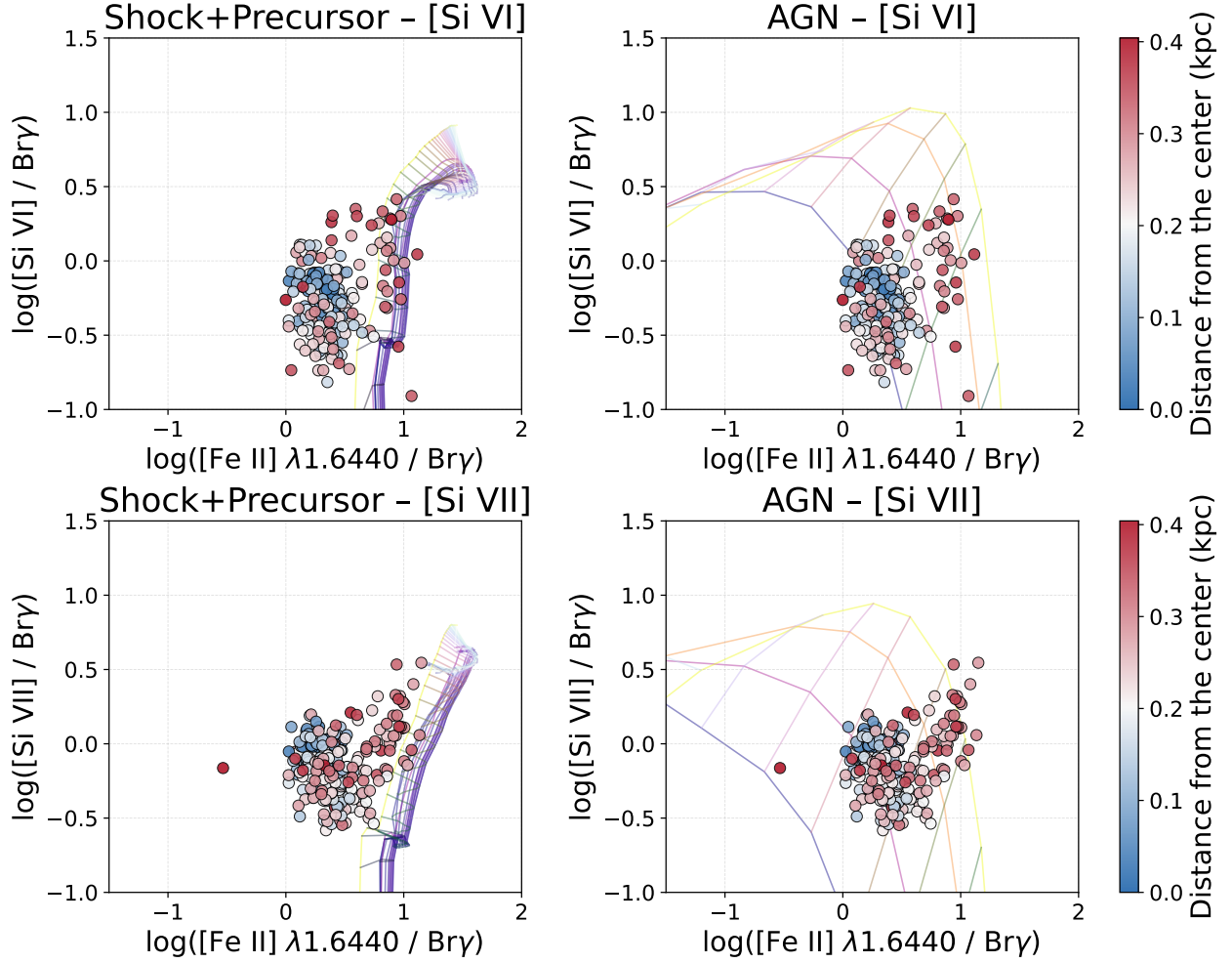


Figure 6. Shock+Precursor model (left) and AGN models (right) for [Si VI] and [Si VII] in J0954. The grid parameters follow the same scheme as in Figure 5 and the color bar indicates the distance from the center in pixels. The ratios in J0954 remain broadly consistent with AGN photoionization even up to 0.4 kpc from the nucleus, with only minor overlap with shock+precursor models.

larger distances, any contribution from shocks is likely small.

5. DISCUSSION

5.1. Non-Uniform Frequency of the Coronal Lines

Previous studies of CLs in dwarf galaxies have found that few systems display all CLs detectable in a given spectral window simultaneously (R. Riffel et al. 2006). The most frequent CLs detections are from Si and S, with the lower-ionization lines (I.P. < 300 eV) typically being stronger. Lines from other elements such as Ca, Al, and Fe are generally weaker and less often detected. Ca and Al can be suppressed by metallicity and depletion onto dust, while Fe may be less affected. Other

CLs, such as those from Mg, have rarely been studied because their wavelengths were largely inaccessible in the pre-JWST era. In massive galaxies, it was initially assumed that the frequency and strength of CLs should depend on the orientation of the torus with respect to the line of sight (T. Murayama & Y. Taniguchi 1998; T. Nagao et al. 2000; J. M. Gelbord et al. 2009), but subsequent work has found little to no difference in the number of detected CLs between Type 1 and Type 2 AGN (R. Riffel et al. 2006; X. Mazzalay et al. 2010; A. Rodríguez-Ardila et al. 2011). The absence of CLs above certain ionization energies may instead point to a softer ionizing continuum. In some cases, higher-I.P. lines are detected while lower-I.P. lines of different species are ab-

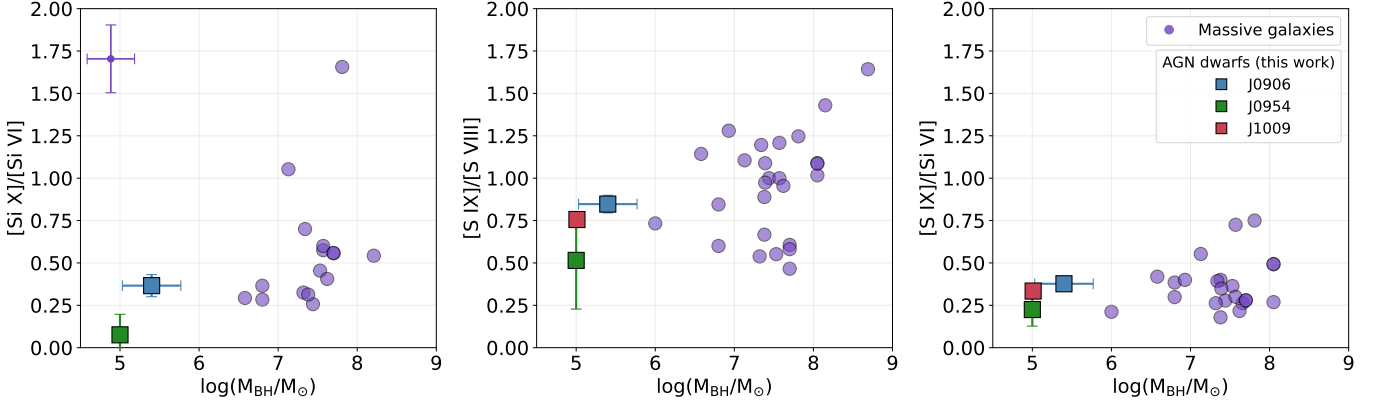


Figure 7. Flux ratios of commonly observed NIR CLs from this work, compared with measurements in massive galaxies from R. Riffel et al. 2006; F. Müller-Sánchez et al. 2011; A. Rodríguez-Ardila et al. 2011; I. Lamperti et al. 2017; M. Bianchin et al. 2024. Black hole masses for the dwarf AGN are taken from the references listed in Table 1. We adopt a uniform uncertainty of 0.5 dex on the black hole masses, based on the average of the quoted errors where available; this is illustrated by the purple error bar in the top left of the first panel. The flux ratios of lines within the same species, [Si X]/[Si VI] (first panel) and [S IX]/[S VIII] (second panel), in dwarf galaxies lie toward the lower end of the distribution compared to those in more massive systems.

sent (I. Lamperti et al. 2017; A. Aravindan et al. 2024), which can be explained by differences in elemental abundances or lack of sensitivity from ground-based NIR instruments. In our sample, we mostly find that, within a given species, there are very few cases where a higher-I.P. line is detected but the corresponding lower-I.P. line is not.

To investigate the origin of the non-uniformity in CL detections, we first examine diagnostics of the ionizing source. J0842 is the only target that falls in the composite region of the BPT diagram when using Keck/LRIS fluxes from C. M. Manzano-King et al. 2019. It may either lack a powerful, hard-spectrum AGN relative to the others, or its AGN signatures may be significantly diluted by stellar contamination. All other targets (J0906, J0954, J1009) lie in the Seyfert region of the BPT diagram (C. M. Manzano-King et al. 2019). Both J0906 and J0954 have strong X-ray detections consistent with AGN activity (V. F. Baldassare et al. 2017), and J0906 additionally hosts a parsec-scale radio jet (J. Yang et al. 2020). J0906 also has the most luminous CLs in our sample, and the median FWHM of its narrow CL component exceeds the median FWHM of both the narrow and broad components in the other three targets, consistent with a powerful central engine and energetic nuclear gas.

J1009 exhibits the richest coronal-line spectrum, with 16 lines detected. As shown in Section 4.2, its $\log U$ values are less negative than those of J0954, likely contributing to the larger number of CLs, including [S XI] (I.P. = 447 eV), which is not detected in J0954. J1009 also has the lowest stellar mass among our targets and, based on black hole–stellar mass relations (A. E. Reines & M. Volonteri 2015), is expected to host a relatively

low-mass black hole. Previous studies have shown that lower-mass black holes are more likely to exhibit multiple strong high-ionization CLs (J. M. Cann et al. 2018). As black hole mass decreases, the Schwarzschild radius decreases and the accretion disk temperature increases, shifting the ionizing continuum to higher energies and enhancing the production of high-ionization lines. The CL detections in J1009 are consistent with this scenario.

Target	$\text{Pa}\alpha/\text{Pa}\beta$	$E(B-V)$	$E(B-V)$ (from $\text{H}\alpha/\text{H}\beta$)
J0842	2.11	0.00	0.00
J0906	2.51	0.44	0.00
J0954	2.48	0.41	0.049
J1009	2.28	0.18	0.166

Table 3. $\text{Pa}\alpha/\text{Pa}\beta$ ratios and extinction values [$E(B-V)$] for the four targets, derived from the narrow component fluxes from the spectra extracted using a $0.3''$ central aperture radius. The extinctions were calculated assuming a Cardelli law with $R_V = 3.1$ and an intrinsic $\text{Pa}\alpha/\text{Pa}\beta$ ratio of 2.133, which is typically assumed for HII regions. Thus, these $E(B-V)$ estimates are uncertain, and do not always agree with extinctions derived assuming an intrinsic ratio of $\text{H}\alpha/\text{H}\beta = 3.1$ (T. Bohn et al. 2021), shown for comparison.

We next consider the role of dust. Balmer decrements (assuming intrinsic ratios suitable for AGN) suggest that these galaxies should not have high dust extinction (W. Liu et al. 2020; T. Bohn et al. 2021). However, the $E(B-V)$ values inferred from the $\text{Pa}\alpha/\text{Pa}\beta$ ratio (Table 3) for J0906 and J0954 are significantly higher; these were derived assuming an intrinsic $\text{Pa}\alpha/\text{Pa}\beta$ ratio of 2.133, more appropriate for H II regions. None of the

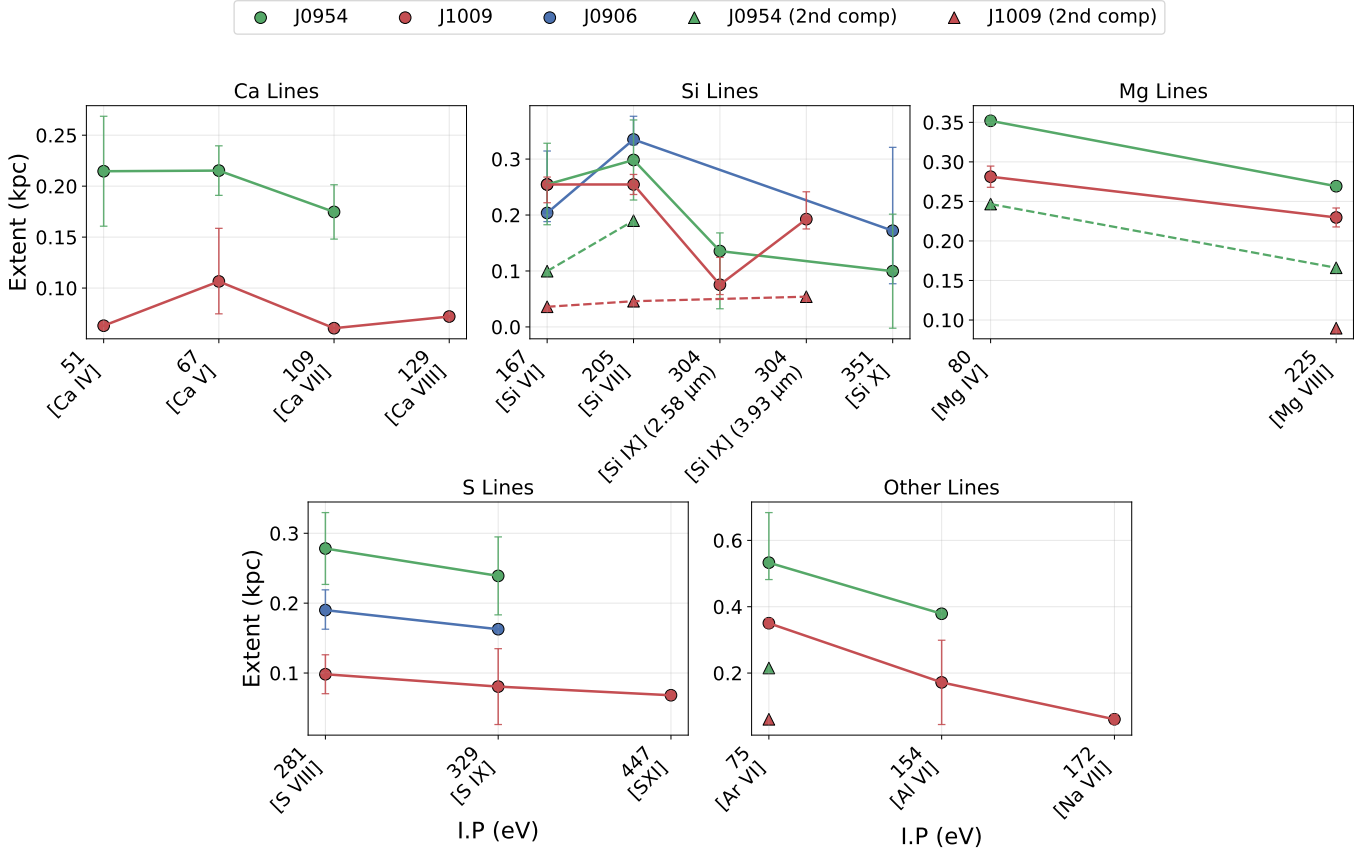


Figure 8. Extents of the various CLs (determined as the radius from the center using the methods outlined in Section 3.4), separated by species, arranged in increasing order of ionization potential on the x-axis. Error bars show asymmetric uncertainties on the CL extents derived from the range of values obtained when varying the S/N threshold used to define significant emission. The solid line indicates the primary component and the dashed line indicates the secondary component, wherever detected. We find that lines with the highest ionization potentials have smaller extents.

four targets show strong large-scale spatial variations between spaxels in their extinction maps.

We also examine flux ratios between CLs of the same ion species as seen in Figure 7. While we do not observe clear systematic trends in the absolute CL fluxes across our sample, the measured line ratios are broadly consistent with those reported in ground-based observations of more massive galaxies. In particular, for commonly identified CLs such as [Si X]/[Si VI] and [S IX]/[S VIII], we find a tentative trend toward smaller line ratios in the AGN dwarfs (Figure 7) compared to higher-mass systems. Although weak, this may indicate a subtle dependence of CL excitation conditions on black hole mass and on less extreme ionizing continua in low-mass systems. Additional ratios using other CLs can be constructed from the fluxes in Appendix B.

5.2. Coronal line region in dwarf galaxies

Determining the size and physical nature of the region where these CLs are formed (the coronal line region; CLR) has long been a challenge. Early work placed

the CLR in a transitional zone between the broad-line region (BLR) and narrow-line region (NLR) (D. Pelat et al. 1981; M. V. Penston et al. 1984; I. N. Evans 1988), but subsequent observations showed that CLs in massive galaxies can extend to hundreds of parsecs, implying that the CLR can span a substantial fraction of the NLR (M. A. Prieto et al. 2005; A. Rodríguez-Ardila et al. 2006; F. Müller-Sánchez et al. 2011; J. Negus et al. 2021).

The extent of a given CL depends on several coupled factors (density, radiation field, abundances, dust, etc.). A full treatment requires detailed photoionization modeling, which we will present in a forthcoming paper. Here we focus on empirical trends in the measured extents.

We use Kendall’s τ (appropriate for our small sample) to test for correlations between ionization potential (I.P.) and the extents (determined using the method listed in Section 3). The element-wise results are weakly consistent with smaller extents for higher-ionization lines, but are not statistically significant (likely due to

the small sample size). Si shows the strongest possible trend ($\tau = -0.64$, $p = 0.055$), S is also negative ($\tau = -1.00$, $p = 0.083$), and Mg and the remaining species show negative τ , while Ca shows no trend ($\tau = -0.11$, $p = 1.00$). The Ca lines despite their relatively low I.P. compared to many other CLs, have among the smallest extents. This might possibly be linked to the strong depletion of Ca onto dust grains at larger radii (B. A. Groves et al. 2004a; J. D. McKaig et al. 2024; W. Matzko et al. 2025), which reduces the gas-phase Ca available for ionization. Pooling all lines in a stratified Kendall’s τ that preserves galaxy identity yields $\tau = -0.20$ ($p = 0.14$, 95% CI $[-0.47, 0.10]$), which is consistent with the same trend but not significant, which may be due to the fact that mixing different elements introduces abundance and depletion effects. Overall, the statistics point toward decreasing spatial extent with increasing I.P., but a larger sample is required for a definitive constraint.

Several of the stronger lines, including [Si VI], [Si VII], [Mg VIII], [Mg IV], and [Ar VI], show larger extents than other CLs and frequently exhibit a second, broader kinematic component. Where multiple components are present, the secondary components have smaller spatial extents than the primary component.

If these weak trends turn out to be real, they might be interpreted in the context of photoionization theory and the density structure of gas around AGN (J. W. Ferguson et al. 1997; A. Rodríguez-Ardila et al. 2011; X. Mazzalay et al. 2013). In ionization-bounded conditions, the CLR size is limited by the available ionizing photons: high-I.P. CLs form closer to the nucleus, while lower-I.P. CLs can be sustained at larger radii. In gas-density-bound conditions, ionizing photons are plentiful but the gas density is too low for efficient collisional excitation into the upper levels, linking the spatial distribution of a line to its critical density n_{crit} . For $n < n_{\text{crit}}$, line emission scales roughly with n^2 , so CLs with higher n_{crit} are preferentially emitted in denser inner regions and lower- n_{crit} lines can extend farther out.

We find no significant correlation between CL extent and n_{crit} . This suggests that the CL extents might be primarily governed by the ionizing radiation field rather than by gas-density limitations. Combined with the results of Section 4.2, this supports a picture in which AGN photoionization dominates the production and radial extent of CLs.

The average CL extent in our sample is $\lesssim 0.5$ kpc (Figure 8). For J0954, the outflow radius of ~ 0.5 kpc inferred from blueshifted UV absorption (C II, C IV, Si II, Si IV) by W. Liu et al. 2024 is consistent with our coronal-line extents, indicating that the CLs might

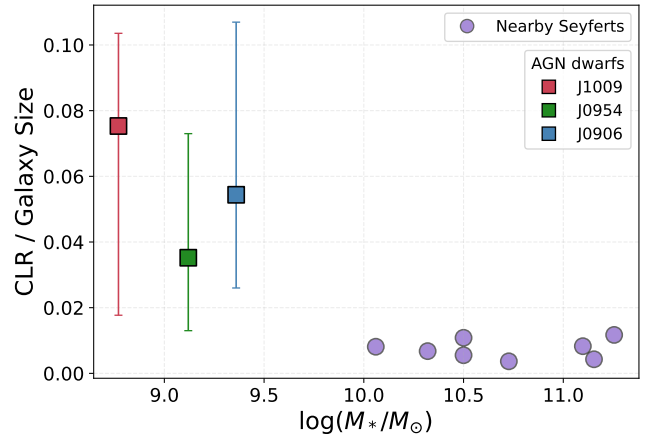


Figure 9. Ratio of the average NIR CL extents to the SDSS r -band isophotal radius as a function of stellar mass, comparing our dwarf galaxies (colored squares) to more massive systems (purple circles; F. Müller-Sánchez et al. 2011; A. Rodríguez-Ardila et al. 2017; D. May et al. 2018). In dwarf galaxies, the CLR can span up to $\sim 10\%$ of the galaxy size, compared to $\sim 1\%$ in massive galaxies.

trace the ionized outflow. When multiple components are present, the broader component has typical extents of ~ 0.1 kpc or less. We can compare our CL extents with measurements in massive galaxies, assuming those have similar sensitivity to our measurements (F. Müller-Sánchez et al. 2011; M. A. Prieto et al. 2005; A. Rodríguez-Ardila et al. 2006). The absolute CL extents in our dwarfs are similar, but because the hosts are smaller, the CLR appears to occupy a larger fraction of the galaxy ($\sim 10\%$ versus $\sim 1\%$). However, optical CLs in massive galaxies have been shown to be more extended (0.7–3 kpc; A. Rodríguez-Ardila et al. 2017; J. Negus et al. 2021; A. Rodríguez-Ardila et al. 2025) so our NIR-based comparison is conservative.

5.3. Correlation with ionized-gas outflows

Although the AGN accretion disk is expected to generate abundant photons capable of producing CLs, recent systematic surveys investigating optical CLs in large samples of nearby galaxies have found such emission to be exceedingly rare within the general galaxy population. This rarity persists even among galaxies identified as AGNs using standard narrow-line ratio diagnostics, at current survey sensitivities (M. Molina et al. 2021; J. Negus et al. 2021; M. Reece et al. 2022; J. Negus et al. 2023). Furthermore, these surveys indicate that CL emission preferentially appears in galaxies with low dust extinction (B. A. Groves et al. 2004a; W. Matzko et al. 2025), suggesting that dust may contribute to suppressing CL emission.

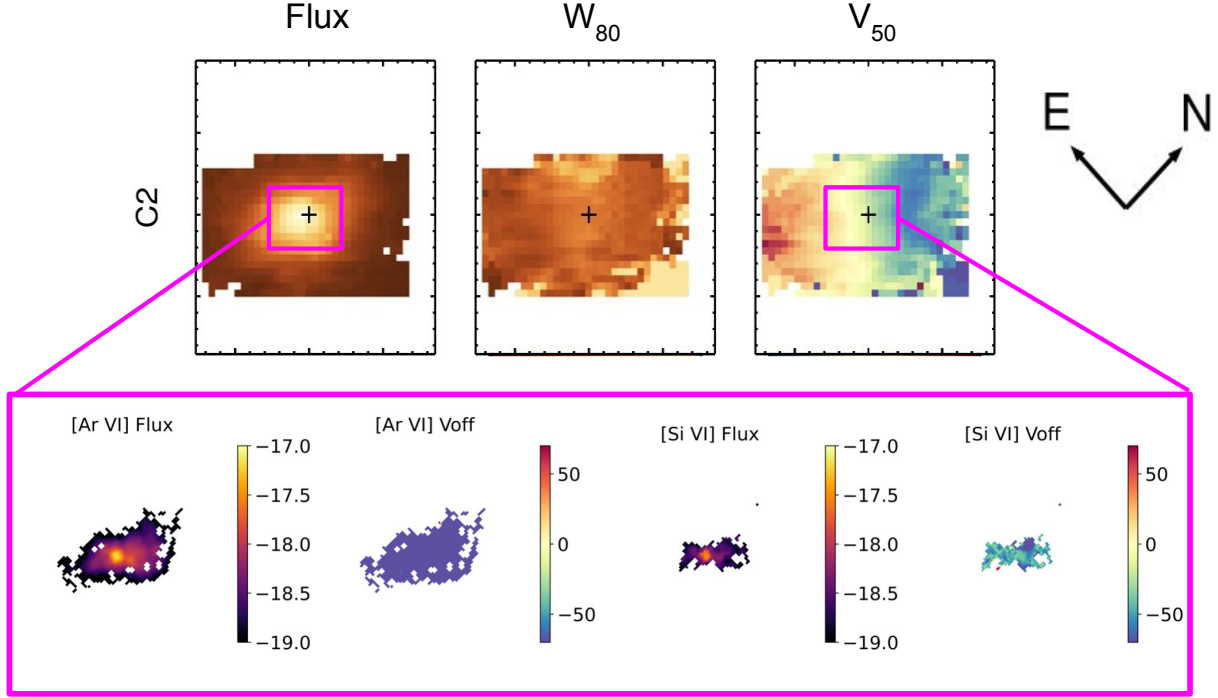


Figure 10. [O III] ionized gas outflow extent in J1009 from KCWI (W. Liu et al. 2020) (top panel) and the corresponding CL extents for two of the CLs from JWST/NIRSpec. The flux maps are in log units of $\text{erg s}^{-1} \text{cm}^{-2} \text{\AA}^{-1}$ and the velocity maps are in km s^{-1} , with the same scale for the CLs as the [O III]. We find that the CL flux maps across all the targets are extended in the same direction as the [O III] ionized gas.

Recent photoionization models by J. D. McKaig et al. 2024 show that gas-phase depletion of refractory elements onto dust grains, along with dust absorption of ionizing photons, can significantly impact CL emission, reducing line luminosities by up to three orders of magnitude compared to dust-free conditions. Consequently, strong CL emission likely occurs only in environments where sufficient grain destruction takes place within highly ionized gas (T. Nagao et al. 2003). All dwarf galaxies with CL in this sample also exhibit low levels of dust extinction in the central regions, at least based on their Balmer decrements (Table 3).

All galaxies in this work show some of the fastest ionized-gas outflows reported in dwarf galaxies, as traced by their broad, blue-shifted [O III] emission-line profiles (C. M. Manzano-King et al. 2019; W. Liu et al. 2020). The [O III] outflow component contributes 5–30% of the total [O III] flux in these galaxies (C. M. Manzano-King et al. 2019). Both J0906 and J0954 require three Gaussian components to model the [O III] emission lines, revealing a broad component with an average FWHM of $\sim 800 \text{ km s}^{-1}$. J0906 and J0954 have maximum outflow velocities of -150 and -80 km s^{-1} , respectively, where the negative sign indicates blue-shifted velocity centroids relative to the systemic velocity. J1009 has a

maximum outflow velocity of -60 km s^{-1} (see also Section 2.1 and Table 1 for more details on the ionized gas outflow properties). The warm ionized-gas mass outflow rates range from $\sim 1\text{--}3 \times 10^{-2} M_{\odot} \text{ yr}^{-1}$, and the kinetic energy outflow rates vary between 1.5×10^{38} to $8 \times 10^{39} \text{ erg s}^{-1}$, which are comparable to those of more luminous AGN in massive systems when normalized by AGN bolometric luminosities.

Outflows could enhance CL emission by clearing out dust from the interior of the galaxies. This was previously suggested in a study of bulgeless galaxies with AGN, where T. Bohn et al. 2022 found that all the galaxies that have AGN-driven outflows also show CL emission, suggesting a correlation between the two. In a systematic study of galaxies with ionized-gas outflows, W. Matzko et al. 2025 showed that galaxies with CL emission exhibit a significantly higher incidence and luminosity of ionized outflows, traced by [O III] $\lambda 5007$, compared to a control sample of non-CL-emitting galaxies. They also found that there exists strong correlations between CL properties (luminosity and FWHM) and outflow velocity. They find that the CL emitters have systematically lower intrinsic extinction toward the ionized gas compared to the controls, supporting a scenario in which dust destruction in AGN-driven outflows

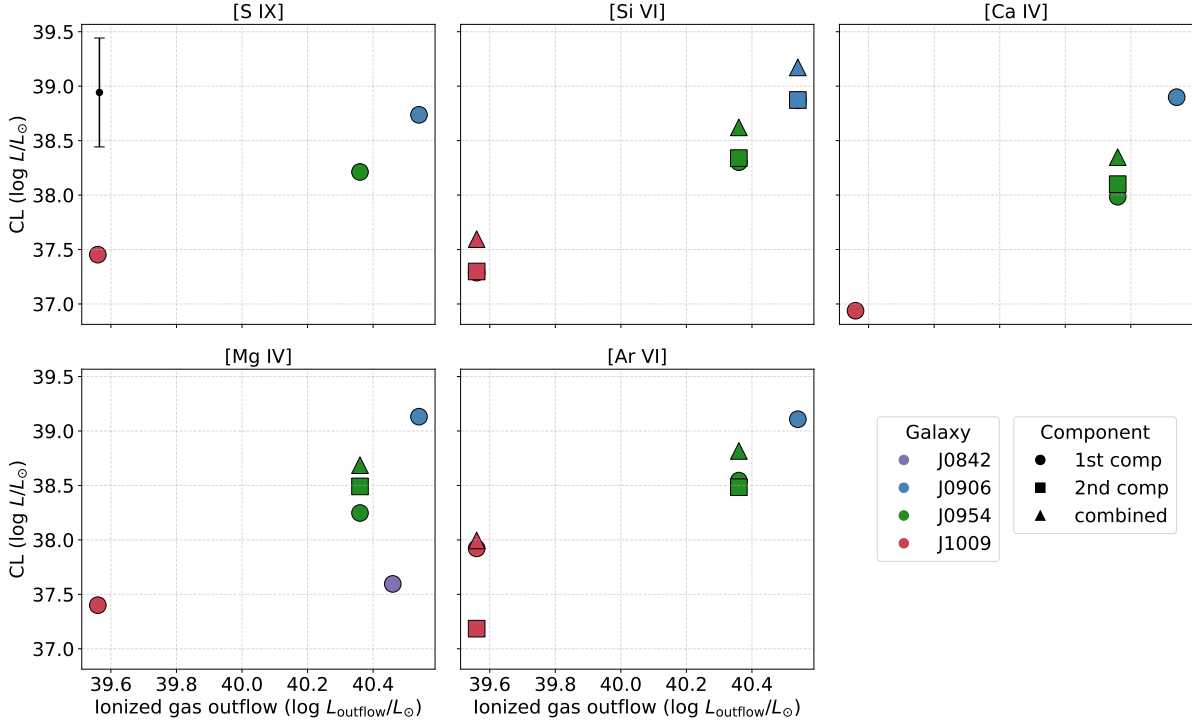


Figure 11. Comparison of the outflow luminosity (calculated from [W. Liu et al. 2020](#)) with CL luminosities. The error is indicated in black in the first panel. Across CL species, the galaxy with the lowest [O III] outflow luminosity (J1009) also exhibits the lowest CL luminosities.

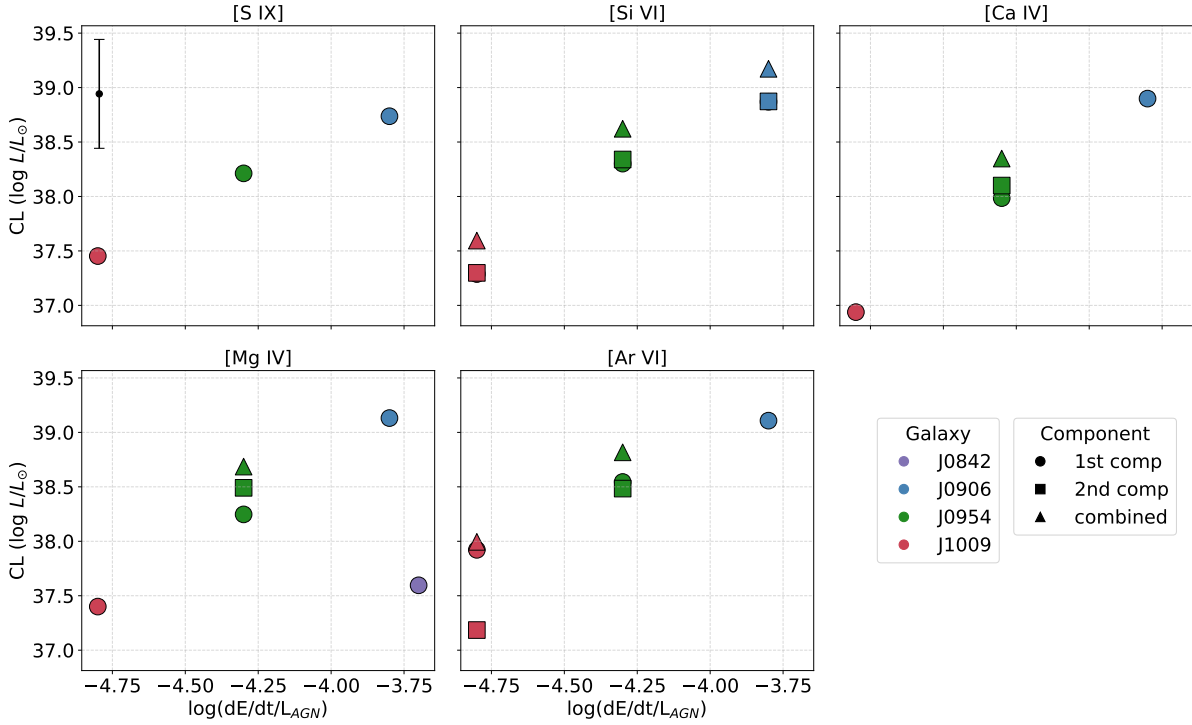


Figure 12. [O III] outflow kinetic energy (normalized by L_{AGN}) vs. CL luminosity. Typical errors are indicated in black in the first panel. We find that the most energetic [O III] outflows tend to have the most luminous CL emission across all CLs.

facilitates efficient CL emission. Although there is a possibility that this correlation is a by-product of AGN power, *W. Matzko et al. 2025* do not find a correlation between the total AGN bolometric luminosity and the CL luminosity (which we also find in this work.)

In our analysis, we also find several correlations between infrared CL properties and the characteristics of ionized gas outflows traced by [O III] (*W. Liu et al. 2020*) in our sample galaxies. The detected CLs are spatially extended along the same direction as the outflows detected in [O III] (Figure 10). The extended CLs also exhibit a largely biconical morphology.

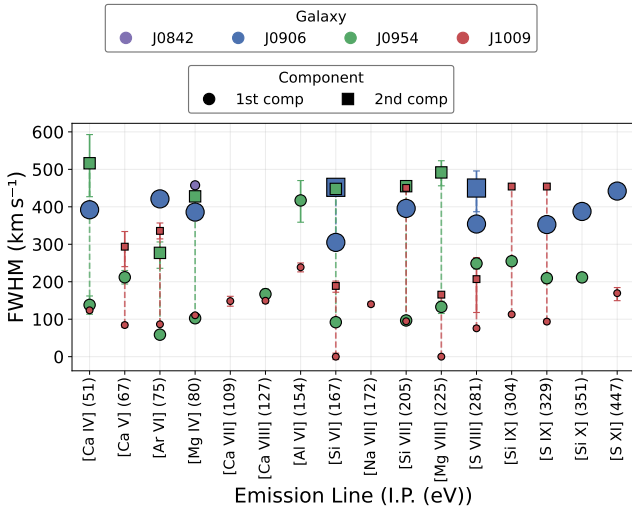


Figure 13. FWHM of the observed CL with the I.P. The size of the marker corresponds to the speed of the [O III] ionized gas outflows in the corresponding galaxy. There is no correlation between the I.P. and FWHM in our sample.

Furthermore, we apply a Kendall’s τ correlation test to determine if a significant correlation exists between the various quantities, such as the CL luminosity and CL FWHM and ionized gas outflow luminosity, [O III] FWHM and the [O III] outflow energetics. The ionized gas outflow luminosity is calculated from the outflow masses given in Table 4 of *W. Liu et al. 2020* using Equation 7 in the same work. The CL luminosities and FWHM are calculated from the integrated spectra using a $0.3''$ central aperture for all the detected CL (we show a subsample of the different CL in Figures 11 and 12, but the correlations are present across all the CLs). We find the strongest correlations (median Kendall’s τ coefficient = 0.42 and p-value = 0.05) between the CL luminosity and the AGN outflow luminosity (Figure 11) as well as between the CL luminosity and the most energetic outflows, given as the kinetic energy injection rate (dE/dt) normalized by the AGN bolometric luminosity

(Figure 12). We do not find a significant correlation between the total AGN bolometric and [O III] luminosities and the CL luminosities. We also find a significant correlation (median Kendall’s τ coefficient > 0.4 and p-value < 0.05) between CL luminosity and the FWHM of the [O III] outflow component. We do not find a significant correlation between the FWHM of CL and that of the [O III] outflow component, which agrees with the results from *W. Matzko et al. 2025*.

While some previous studies have suggested that CLs with higher I.P. tend to exhibit broader profiles (*A. Rodríguez-Ardila et al. 2002; L. Armus et al. 2023*), we do not find a statistically significant correlation between either FWHM or W_{80} and the I.P. or the critical density (n_{crit}) of the lines (Figure 13). However, we do find that targets with larger W_{80} values in the broad [O III] component also show correspondingly large W_{80} values across their CLs (Figure 13).

Although the limited size of our sample makes it difficult to characterize broader trends, our results are consistent with previous studies suggesting that outflows may play a role in dust destruction, thereby enabling efficient CL detection.

5.4. Outflows traced by Coronal Lines

We find that several CLs in the observed dwarf galaxies have a second, broad component suggestive of possible outflow. While CL broadening may reflect AGN activity, the presence of outflows detected by the [O III] lines necessitates investigating whether even the highest-ionization gas participates in the outflow. The velocity offsets of the broad CL range from -150 to 150 km s^{-1} , with W_{80} values ranging from $300 - 500 \text{ km s}^{-1}$. We find that, overall, the broad CL components have smaller velocities as compared to lines such as [S III] ($0.9533 \mu\text{m}$) and He II ($1.0125 \mu\text{m}$), which have similar I.P.s and n_e to [O III]. A more detailed analysis of outflows in other lines will be presented in a future study.

Assuming the secondary component seen in the CLs is an outflow, we can derive standard estimates of energetics, including the mass outflow and kinetic energy rates. Previous studies on CL energetics (*F. Müller-Sánchez et al. 2011; A. Rodríguez-Ardila et al. 2017*) account for the velocities and the extents of the outflow. However, they do not measure the mass from the luminosities of the CL, but instead assume a certain filling factor and make use of the hydrogen mass alone. The unknown filling factor leads to large uncertainties in the calculated energetics. In this work, we make use of [Si VI] luminosities in order to estimate the amount of gas mass present in the outflow, and use that to determine the outflow energetics (see Appendix A for a more detailed deriva-

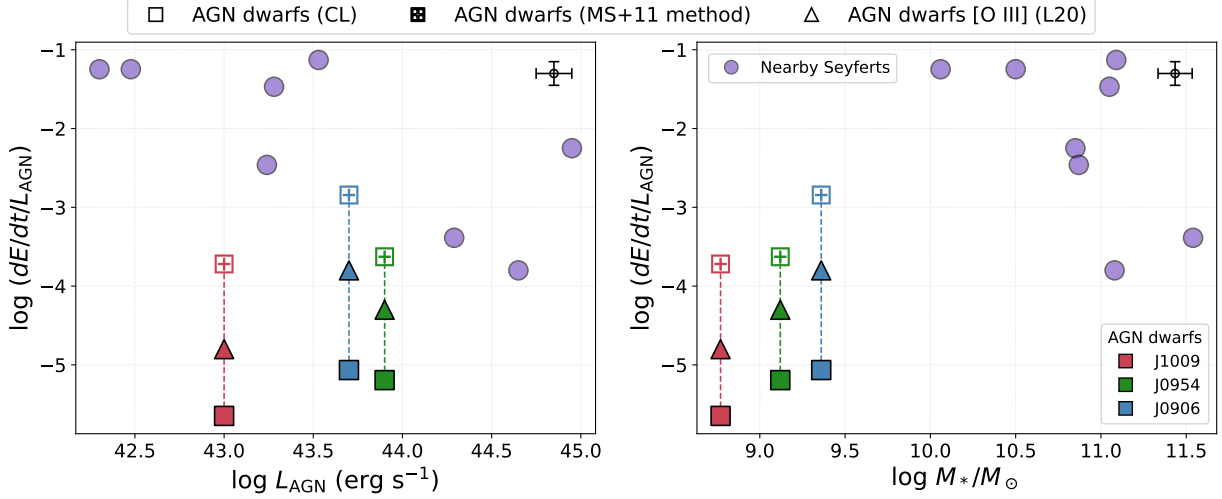


Figure 14. Kinetic energy outflow rates (see Equation (5)) normalized to the AGN luminosity as a function of AGN luminosity (left) and stellar mass (right). The colored (red, green, blue) points indicate AGN dwarfs and the purple circles indicate measurements from nearby Seyferts (F. Müller-Sánchez et al. 2011; A. Rodríguez-Ardila et al. 2017; D. May et al. 2018) with spatially resolved NIR CL measurements. The squares indicate measurements for [Si VI] using Equations (2) - (5) and the triangles are from [O III] (W. Liu et al. 2020). The squares with crosses indicate energetics calculated assuming a filling factor using equations from F. Müller-Sánchez et al. 2011, also used in A. Rodríguez-Ardila et al. 2017. Across the sample, coronal-line-based outflow energetics are 0.5–1.0 dex higher than those of [O III].

tion). We use the following equation to derive the mass outflow rates for a steady state-outflow:

$$M_{\text{coronal gas}} = 160 M_{\odot} \left(\frac{L_{[\text{Si VI}], \text{ext. corr}}}{10^{35} \text{ erg s}^{-1}} \right) \left(\frac{n_e}{100 \text{ cm}^{-3}} \right)^{-1} \quad (2)$$

where $L_{[\text{Si VI}], \text{ext. corr}}$ is the extinction-corrected [Si VI] luminosity and n_e is the electron density, measured from the [SII] $\lambda\lambda 6716, 6731$ line ratios, obtained from Gemini/GMOS spectra or Keck/LRIS spectra (W. Liu et al. 2020). We caution that the n_e we adopt from the [SII] doublet likely traces lower-ionization NLR gas rather than the coronal line-emitting region itself (D. Baron & H. Netzer 2019; R. Davies et al. 2020). If the CLR is denser than the [SII]-emitting gas, our assumed n_e is underestimated and the inferred outflow masses and rates should be treated as upper limits.

The calculations of the mass, momentum, and kinetic energy outflow rates depend on the spatial extent of the outflows which we calculate in Section 3.4 and discuss in Section 5.2. Specifically, the energetics are calculated by summing up quantities over individual spaxels:

$$dM/dt = \sum dm/dt = \sum \frac{m_{\text{out}} v_{\text{off, out}} \sec \theta}{R_{\text{out}}} \quad (3)$$

$$dp/dt = \sum (v_{\text{off, out}} \sec \theta) dm/dt \quad (4)$$

$$dE/dt = \frac{1}{2} \sum [(v_{\text{off, out}} \sec \theta)^2 + 3\sigma_{\text{out}}^2] dm/dt, \quad (5)$$

where m_{out} is the outflowing mass in each spaxel, $v_{\text{off, out}}$ is the value of v_{off} in each spaxel, and σ_{out} is the velocity dispersion calculated as $W_{80}/2.73$. R_{out} is the radial extent of the outflow. θ is the angle between the velocity vector of the outflow in 3D space and the line of sight, defined as $\theta = \sin^{-1}(r_{\text{spaxel}}/R_{\text{out}})$.

The calculated energetics, along with the average velocity offsets, W_{80} and the extents R_{out} used in the calculations of the energetics are given in Table 4.

In Figure 14, we plot the mass and kinetic energy outflow rates estimated for the outflowing gas traced by the CLs as a function of mass and AGN luminosity. We also compare the outflow rates from CL to the ionized [O III] gas measurements and find that the CL outflow rates are 1 dex lower, which could be due to underestimating the W_{80} values due to the de-wiggling process (see Section 3.3). We also compare the energetics measured in this work to energetics calculated using [Si VI] outflows from ground-based low- z Seyferts (F. Müller-Sánchez et al. 2011; A. Rodríguez-Ardila et al. 2017; D. May et al. 2018). Since the mass outflow rates in these works were calculated assuming a filling factor, we also calculated the energetics from the AGN dwarfs using the equations presented in F. Müller-Sánchez et al. 2011 (indicated by the boxes with a cross). We assume a filling factor (0.001) similar to F. Müller-Sánchez et al. 2011 and find that this measurement over estimates the values for energetics by at least two orders of magnitude. Even if we assume higher n_e and filling factor values

Table 4. Energetics of the gas, traced by the [Si VI] line

Name	Comp	n_e (cm^{-3})	R_{out} (kpc)	Avg. v_{off} (km s^{-1})	Avg. W_{80} (km s^{-1})	$\log(M_{out})$ (M_\odot)	$\log[(dM/dt)]$ ($M_\odot \text{ yr}^{-1}$)	$\log[(dE/dt)]$ (erg s^{-1})	$\log[(c dp/dt)]$ (L_\odot)
(1)	(2)	(3)	(4)	(5)	(6)	(7)	(8)	(9)	(10)
J0906	1	570 ± 360	0.203	30 ± 16	337 ± 43	$5.27^{+0.6}_{-0.9}$	$-1.70^{+0.5}_{-0.4}$	$38.63^{+0.5}_{-0.5}$	$7.67^{+0.3}_{-0.5}$
J0954	1	470 ± 80	0.254	-6 ± 12	138 ± 39	$4.69^{+0.1}_{-0.2}$	$-2.73^{+0.1}_{-0.2}$	$36.76^{+0.1}_{-0.2}$	$6.23^{+0.1}_{-0.2}$
	2	470 ± 80	0.099	60 ± 24	405 ± 43	$4.34^{+0.3}_{-0.3}$	$-1.81^{+0.3}_{-0.3}$	$38.70^{+0.3}_{-0.3}$	$7.99^{+0.3}_{-0.3}$
J1009	1	150 ± 60	0.254	-45 ± 13	145 ± 40	$4.50^{+0.2}_{-0.2}$	$-2.75^{+0.2}_{-0.2}$	$37.07^{+0.2}_{-0.2}$	$6.59^{+0.2}_{-0.2}$
	2	150 ± 60	0.037	-45 ± 13	343 ± 35	$3.65^{+0.2}_{-0.2}$	$-3.01^{+0.2}_{-0.2}$	$37.35^{+0.2}_{-0.2}$	$6.13^{+0.2}_{-0.2}$

NOTE—Column (1): Short name of the target. Column (2): Individual outflow components from the best fits. Column (3): Electron density measured from the [SII] $\lambda\lambda 6716, 6731$ line ratio based on the total line flux from the spatially integrated, Gemini/GMOS spectra or Keck/LRIS spectra (see W. Liu et al. 2020). Column (4): Outflow radius adopted in the calculation of mass, momentum, and kinetic energy outflow rates when the outflows are spatially resolved. Column (5): Average offset velocity calculated from the best fits. Column (6): Average W_{80} calculated from the best fits. Column (7): Ionized gas mass of the corresponding outflow component. Column (8): Ionized gas mass outflow rate of the corresponding outflow component. Column (9): Ionized gas kinetic energy outflow rate of the corresponding outflow component. Column (10): Ionized gas momentum outflow rate of the corresponding velocity component

suitable for dwarf galaxies, the energetics are still found to be higher. This could indicate that the filling factors for CL are much lower than previously assumed.

Because the highly ionized phase of the gas traced by CLs appears neither fast nor radially extended, it likely cannot expel gas from the galaxy. However, its energetics may be sufficient to disturb gas in the central regions, potentially contributing to feedback-driven gas redistribution that has been invoked to produce cored (rather than cuspy) dark-matter profiles in dwarf galaxies (W. J. G. de Blok 2010). They might also accelerate gas and redistribute mass in the central, high-gravitational-potential regions, potentially driving more extended, lower-ionization outflows (e.g., [O III]).

6. SUMMARY AND CONCLUSIONS

Using JWST/NIRSpec, we undertake the *first* spatially resolved examination of NIR coronal lines in dwarf galaxies with AGN and ionized-gas outflows to address the challenges in unambiguously identifying AGN activity and assessing AGN-driven feedback in these low-mass systems. We generate spatial maps of the flux and velocity of the different coronal lines, allowing us to examine in detail the influence of AGN feedback, as traced by the coronal lines, on the host dwarf galaxies. We present our main results as follows:

- 16 different species of near-infrared coronal lines were detected across four dwarf galaxies, tripling the number of detected CL transitions in dwarf galaxies compared to previous ground-based studies. The galaxy with the lowest stellar mass

(J1009, $M_* = 10^{8.77} M_\odot$, about 2.5 times less massive than the other dwarf galaxies in the observed sample) exhibits the maximum number of CLs (15) among all the galaxies, indicating that black holes in small dwarf galaxies are capable of producing the ionization required to form CLs.

- Based on shock and AGN models, we find that AGN photoionization is largely responsible for producing CLs. J1009, in particular, is dominated by AGN photoionization with minimal to no contribution from shock ionization to producing the CLs. The models also suggest that J1009 is hosting a highly accreting, low-mass black hole that is capable of producing numerous CL with I.P.s as high as 447 eV.
- The average extents of the CLs across the four dwarf galaxies are ~ 0.5 kpc, which is similar to the extents found tracing NIR CL in massive galaxies. The small sizes of dwarf galaxies mean their CLRs can occupy $\sim 10\%$ of the host galaxy, about ten times the fractional extent seen in massive galaxies. In J0954, an outflow radius of ~ 0.5 kpc estimated from blueshifted UV absorption (W. Liu et al. 2024) agrees with the CL extents, supporting CLs as tracers of the ionized outflow.
- The presence, extent, and luminosity of the CLs correlate with the properties of the ionized gas outflows traced by [O III]. In galaxies with spatially resolved CL emission, CLs exhibit biconi-

cal structure, align with the outflow axis, consistent with an AGN-powered outflow. The CL luminosities correlate with both the ionized gas outflow luminosities and the FWHM of the outflows. Two of the galaxies with CL detections also have small dust extinction values, suggesting that AGN-driven outflows may enhance CL emission by clearing dust from the nuclear regions.

- Several CLs exhibit wings, suggestive of a possible secondary kinematic component. If this is an outflow, energy estimates imply this highly ionized gas can have a dynamical impact on the gas near galaxy centers.

The results confirm that the outflows detected in these dwarf galaxies are predominantly AGN-powered and that CLs may trace their presence and impact. By revealing signatures of dust clearing, gas heating, and kinematically distinct ionized outflows, CLs may provide a direct view of how AGN in dwarf galaxies can exert feedback, potentially influencing their evolution. Our findings highlight the potential for CLs as diagnostics of AGN activity in low-mass, dust-poor environments, which are conditions reminiscent of galaxies in the early universe. With increased observations of AGN in faint galaxies at high redshifts (J. Brinchmann 2023; L. J. Furtak et al. 2023; Y. Harikane et al. 2023; D. D. Kocevski et al. 2023; I. Labbé et al. 2023; R. Maiolino et al. 2024), including detections of CLs such as [Ne V] in dwarf galaxies at the epoch of reionization (J. Chisholm et al. 2024) using JWST, understanding the formation and detection of CLs in dwarf galaxies is critical. Given that local dwarf galaxies are crucial analogs for understanding the formation and evolution of the earliest galaxies in the high-redshift universe, where they are increasingly recognised as key drivers of reionization (H. Atek et al. 2024) and where AGN feedback in dwarf galaxies is gaining importance in galaxy quenching (E.

Arjona-Gálvez et al. 2024), these results provide invaluable empirical constraints for cosmological simulations and future JWST observations aimed at unveiling the role of AGN in early galaxy evolution.

ACKNOWLEDGMENTS

This work is based on observations made with the NASA/ESA/CSA James Webb Space Telescope. The data were obtained from the Mikulski Archive for Space Telescopes at the Space Telescope Science Institute, which is operated by the Association of Universities for Research in Astronomy, Inc., under NASA contract NAS 5-03127 for JWST. These observations are associated with program #3663. Support for program #3663 was provided by NASA through a grant from the Space Telescope Science Institute. All the *JWST* data used in this paper can be found in MAST doi: [10.17909/19nr-xp61](https://doi.org/10.17909/19nr-xp61). VU acknowledges partial funding support from NSF AAG grant #2536603 and NASA ADSPS grant #80NSSC25K0169. MB acknowledges support from the Juan de La Cierva scholarship with reference JDC2023–052684–I, funded by MICIU/AEI/10.13039/501100011033 and from the Agencia Estatal de Investigación of the Ministerio de Ciencia, Innovación y Universidades (MCIU/AEI) under the grant “Tracking active galactic nuclei feedback from parsec to kiloparsec scales”, with reference PID2022–141105NB–I00 and the European Regional Development Fund (ERDF). We thank Danielle Berg and Zorayda Martinez for helpful discussions regarding this work.

Facilities: JWST(NIRSpec)

Software: astropy (Astropy Collaboration et al. 2013, 2018, 2022), BADASS (R. O. Sexton et al. 2021), pPXF, (M. Cappellari & E. Emsellem 2004), PyNeb (V. Luridiana et al. 2015),

APPENDIX

A. OUTFLOW ENERGETICS

Spatially resolved IFU data has proven to be integral to deriving various energetics of outflows (the amount of mass carried by the outflows, the rates of mass, momentum and kinetic energy of the outflow), by providing constraints on the spatial extent of the outflow, which is a crucial factor in the calculation of the energetics. The energetics are dependent on several assumptions, such as the shape of the outflow (spherical vs. biconical). The ionized gas mass of the outflows can be calculated based on either the [O III] λ , λ 4959, 5007 line luminosity or the Balmer line ($H\alpha$ or $H\beta$) luminosity of the outflowing, line emitting gas. Calculating the coronal gas mass using CLs is challenging. Previous works (F. Müller-Sánchez et al. 2011; A. Rodríguez-Ardila et al. 2017; D. May et al. 2018; A. Rodríguez-Ardila & M. A. Fonseca-Faria 2020), typically assume a spherically symmetric outflow with a certain filling factor, with only

the outflow velocities and the spatial extent as the varying parameters, and do not account for the gas mass from the luminosity of the CL. We find that this method assuming a filling factor typically overestimates the mass and kinetic energy outflow rates (Figure 14). Since the luminosity of the CLs give us the best estimate of the coronal ionized gas mass in the galaxy, in this work, we derive the coronal ionized gas mass using the luminosity of the [Si VI] CL, following the methods from [D. E. Osterbrock & G. J. Ferland 2006](#); [S. Veilleux et al. 2020](#); [W. Liu et al. 2020](#), assuming a case B recombination.

The luminosity of [Si VI] can be given as

$$L_{\text{Si VI}} = \int j_{[\text{Si VI}]} dV \quad (\text{A1})$$

where $j_{[\text{Si VI}]}$ is the line emissivity coefficient and can be written as:

$$j_{[\text{Si VI}]} = n_e n_{[\text{Si VI}]} \epsilon_{[\text{Si VI}]}(T_e, N_e) \quad (\text{A2})$$

where n_e is the electron density, $n_{[\text{Si VI}]}$ is the number density of [Si VI] and $\epsilon_{[\text{Si VI}]}$ is the line emission coefficient.

The total coronal gas mass associated with [Si VI], M_{cor} , is primarily hydrogen and helium. Si is only a trace element. So, to convert [Si VI] density into a total mass, we assume a certain abundance ratio A_{Si} :

$$A_{\text{Si}} = \frac{n_{\text{Si}}}{n_{\text{H}}} \quad (\text{A3})$$

Considering the ionization fraction of [Si VI] $f_{[\text{Si VI}]}$,

$$f_{[\text{Si VI}]} = \frac{n_{[\text{Si VI}]}}{n_{\text{Si}}} \quad (\text{A4})$$

We can now find the number density of hydrogen n_{H} :

$$n_{\text{H}} = \frac{n_{[\text{Si VI}]}}{A_{\text{Si}} f_{[\text{Si VI}]}} \quad (\text{A5})$$

The total coronal gas mass is given as:

$$M_{\text{cor}} = m_p \int n_{\text{H}} dV = m_p \int \frac{n_{[\text{Si VI}]}}{A_{\text{Si}} f_{[\text{Si VI}]}} dV \quad (\text{A6})$$

Multiplying the numerator and denominator with constants $n_e \epsilon_{[\text{Si VI}]}$:

$$M_{\text{cor}} = m_p \int \frac{n_e n_{[\text{Si VI}]} \epsilon_{[\text{Si VI}]}}{A_{\text{Si}} f_{[\text{Si VI}]} n_e \epsilon_{[\text{Si VI}]}} dV = \frac{m_p}{A_{\text{Si}} f_{[\text{Si VI}]} n_e \epsilon_{[\text{Si VI}]}} \int n_e n_{[\text{Si VI}]} \epsilon_{[\text{Si VI}]} dV \quad (\text{A7})$$

Replacing the term under the integral with A1 and A2.

$$M_{\text{cor}} = \frac{m_p L_{[\text{Si VI}]}}{A_{\text{Si}} f_{[\text{Si VI}]} n_e \epsilon_{[\text{Si VI}]}} \quad (\text{A8})$$

where the values of constants are

- Mass of the proton: $m_p = 1.67 \times 10^{-24}$ g
- The abundance ratio is obtained from [M. Asplund et al. 2009](#) assuming a solar abundance: $A_{\text{Si}} = 3.24 \times 10^{-5}$
- The ionization fraction of [Si VI] is assumed to be 0.5: $f_{[\text{Si VI}]} = 0.5$. This is taken as a conservative upper limit and we find that for lower $f_{[\text{Si VI}]}$, the change in the energetics is comparable to the errors listed in Table 4.
- $\epsilon_{[\text{Si VI}]}$ is determined using the line emission code PyNeb ([V. Luridiana et al. 2015](#)) using the CHIANTI atomic database ([K. P. Dere et al. 1997](#); [G. Del Zanna et al. 2021](#)) using an electron temperature of 20000 K (which is the average temperatures of the gas traced by CL ([J. Negus et al. 2021](#))) and electron density of 100 cm^{-3} : $\epsilon_{[\text{Si VI}]} = 3.26 \times 10^{-21} \text{ erg cm}^3 \text{ s}^{-1}$

The calculations of the mass, momentum, and kinetic energy outflow rates depend on the above derived ionized gas mass and the spatial extent of the outflows and are given in Section 5.4.

B. CORONAL LINE FLUXES AND FWHM

The coronal line fluxes and the FWHM for all the four targets. We find the total line fluxes by summing over the flux values in the fitted spatial maps and also present the extinction-corrected values. For the lines which could not be detected with sufficient S/N ratio in the individual spaxels, we fit the emission line by integrating a spectrum over a $0.3''$ aperture radius and report the total integrated flux. The average FWHM is the average of the FWHM values in the fitted spatial maps, or the value of FWHM in the integrated spectrum. We determined that the significant contribution to the error in the measured fluxes were primarily from the stellar component fitted using various stellar templates, and we report the error based off the flux determined from the fit without the stellar template. The upper limits for non-detected lines were estimated from the local continuum noise. For each line, we assumed an unresolved Gaussian profile with a FWHM set equal to the average FWHM of the detected emission lines in the same spectrum. The continuum level was measured from nearby line-free regions, and the noise was quantified using the median absolute deviation of the residuals after continuum subtraction. This 1σ noise level was then scaled to 3σ , and the resulting 3σ integrated flux upper limits are reported in the final column of the tables.

Table 5. Coronal line fluxes for J0842

Coronal line (Wavelength)	Flux	Flux (Extinction corrected)	FWHM	Flux Upper-limits	Notes
	(10^{-20} W m $^{-2}$)	(10^{-20} W m $^{-2}$)	(km s $^{-1}$)	(10^{-20} W m $^{-2}$)	
(1)	(2)	(3)	(4)	(5)	(6)
[S VIII] (0.9911 μ m)	0.19	Non-detection
[S IX] (1.2520 μ m)	0.08	Non-detection
[Si X] (1.4301 μ m)	1.07	Non-detection
[S XI] (1.9220 μ m)	0.25	Non-detection
[Si VI] (1.9630 μ m)	0.34	Non-detection
[Ca VIII] (2.3205 μ m)	0.70	Non-detection
[Si VII] (2.4826 μ m)	0.33	Non-detection
[Si IX] (2.5839 μ m)	0.23	Non-detection
[Mg VIII] (3.0276 μ m)	0.26	Non-detection
[Ca IV] (3.2061 μ m)	0.14	Non-detection
[Al VI] (3.6593 μ m)	0.23	Non-detection
[Si IX] (3.9357 μ m)	1.19	Non-detection
[Ca VII] (4.0864 μ m)	0.18	Non-detection
[Ca V] (4.1574 μ m)	0.25	Non-detection
[Mg IV] (4.4871 μ m)	1.01 ± 0.05	1.01	264 ± 66
[Ar VI] (4.5280 μ m)	0.26	Non-detection
[Na VII] (4.6834 μ m)	0.43	Non-detection

NOTE—Column (1): Coronal line species and rest wavelength. Column (2): Observed flux. Column (3): Extinction-corrected flux. Column (4): Average FWHM. Column (5): Upper limits for non-detections. Column (6): Notes on detections.

Table 6. Coronal line fluxes for J0906

Coronal line (Wavelength)	Flux	Flux (Extinction corrected)	FWHM	Flux Upper-limits	Notes
	(10^{-20} W m $^{-2}$)	(10^{-20} W m $^{-2}$)	(km s $^{-1}$)	(10^{-20} W m $^{-2}$)	
(1)	(2)	(3)	(4)	(5)	(6)
[S VIII] (0.9911 μ m)	9.89 ± 2.34	11.8	334 ± 34
[S IX] (1.2520 μ m)	8.39 ± 2.50	10.0	315 ± 37
[Si X] (1.4301 μ m)	8.12 ± 0.99	9.71	281 ± 30
[S XI] (1.9220 μ m)	6.80 ± 1.54	8.13	455 ± 11	...	Int. spectrum
[Si VI] (1.9630 μ m)	21.90 ± 6.52	26.5	311 ± 40
[Ca VIII] (2.3205 μ m)	Detector gap
[Si VII] (2.4826 μ m)	19.68 ± 8.67	23.5	320 ± 52
[Si IX] (2.5839 μ m)	0.65	Non-detection
[Mg VIII] (3.0276 μ m)	27.14 ± 6.63	32.5	338 ± 46
[Ca IV] (3.2061 μ m)	15.30 ± 0.47	18.3	398 ± 20	...	Int. spectrum
[Al VI] (3.6593 μ m)	2.66	Non-detection
[Si IX] (3.9357 μ m)	Detector gap
[Ca VII] (4.0864 μ m)	2.61	Non-detection
[Ca V] (4.1574 μ m)	5.15 ± 3.52	6.16	140 ± 17	...	Int. spectrum
[Mg IV] (4.4871 μ m)	26.40 ± 4.77	31.6	402 ± 15	...	Int. spectrum
[Ar VI] (4.5280 μ m)	25.00 ± 5.78	29.9	431 ± 18	...	Int. spectrum
[Na VII] (4.6834 μ m)	1.52	Non-detection

NOTE—Same as Table 5, but for J0906. The ‘Int. spectrum’ note indicates that the line is detected only in the integrated spectrum extracted from the central 0.3'' aperture.

Table 7. Coronal emission line fluxes for J0954

Coronal line (Wavelength)	Flux	Flux (Extinction corrected)	FWHM	Flux Upper-limits	Notes
	(10^{-20} W m $^{-2}$)	(10^{-20} W m $^{-2}$)	(km s $^{-1}$)	(10^{-20} W m $^{-2}$)	
(1)	(2)	(3)	(4)	(5)	(6)
[S VIII] (0.9911 μ m)	6.45 ± 0.46	7.61	215 ± 57
[S IX] (1.2520 μ m)	3.32 ± 2.09	3.92	155 ± 37
[Si X] (1.4301 μ m)	1.12 ± 1.00	1.32	63 ± 89
[S XI] (1.9220 μ m)	0.08	Non-detection
[Si VI] (1.9630 μ m)	14.71 ± 2.88	17.40
(Narrow)	10.30 ± 2.58	12.20	127 ± 36
(Broad)	4.41 ± 0.30	5.20	374 ± 40
[Ca VIII] (2.3205 μ m)	3.16 ± 1.01	3.73	167 ± 13	...	Int. spectrum
[Si VII] (2.4826 μ m)	22.10 ± 7.54	26.00
(Narrow)	12.00 ± 3.77	14.10	114 ± 37
(Broad)	10.10 ± 3.77	11.90	396 ± 51
[Si IX] (2.5839 μ m)	4.85 ± 3.37	5.73	221 ± 45
[Mg VIII] (3.0276 μ m)	16.65 ± 5.76	19.68
(Narrow)	10.90 ± 4.83	12.90	185 ± 45
(Broad)	5.75 ± 2.73	6.78	375 ± 47
[Ca IV] (3.2061 μ m)	7.20 ± 2.17	8.50	177 ± 52
[Al VI] (3.6593 μ m)	2.44 ± 2.15	2.88	226 ± 68
[Si IX] (3.9357 μ m)	Detector gap
[Ca VII] (4.0864 μ m)	1.21 ± 0.38	1.43	173 ± 71
[Ca V] (4.1574 μ m)	5.10 ± 2.04	6.02	158 ± 48
[Mg IV] (4.4871 μ m)	12.81 ± 3.87	15.05
(Narrow)	10.40 ± 3.67	12.20	114 ± 39
(Broad)	2.41 ± 0.20	2.85	242 ± 63
[Ar VI] (4.5280 μ m)	27.02 ± 5.38	31.96	60 ± 26
(Narrow)	21.80 ± 2.69	25.80	60 ± 26
(Broad)	5.22 ± 2.69	6.16	198 ± 48
[Na VII] (4.6834 μ m)	1.70	Non-detection

NOTE—Column (1): Coronal line species and rest wavelength. Column (2): Observed flux. Column (3): Extinction-corrected flux. Column (4): Average FWHM. Column (5): Upper limits for non-detections. Column (6): Notes on special cases (non-detections, detector gaps, or integrated spectra. The ‘Int. spectrum’ note indicates that the line is detected only in the integrated spectrum extracted from the central 0.3'' aperture). For multi-component fits, Narrow and Broad entries are listed separately beneath the total flux row.

Table 8. Coronal emission line fluxes for J1009

Coronal line (Wavelength)	Flux	Flux (Extinction corrected)	FWHM	Flux Upper-limits	Notes
	(10^{-20} W m $^{-2}$)	(10^{-20} W m $^{-2}$)	(km s $^{-1}$)	(10^{-20} W m $^{-2}$)	
(1)	(2)	(3)	(4)	(5)	(6)
[S VIII] (0.9911 μ m)	6.36 ± 0.81	6.85	243 ± 58
[S IX] (1.2520 μ m)	4.82 ± 0.56	5.18	124 ± 38
[Si X] (1.4301 μ m)	Detector gap
[S XI] (1.9220 μ m)	1.19 ± 0.58	1.28	192 ± 49
[Si VI] (1.9630 μ m)	14.45 ± 2.60	15.48
(Narrow)	12.80 ± 2.30	13.70	134 ± 37
(Broad)	1.65 ± 0.30	1.78	317 ± 32
[Ca VIII] (2.3205 μ m)	1.87 ± 0.29	2.01	150 ± 38
[Si VII] (2.4826 μ m)	19.78 ± 3.63	21.26
(Narrow)	17.40 ± 2.28	18.70	102 ± 28
(Broad)	2.38 ± 1.35	2.56	466 ± 106
[Si IX] (2.5839 μ m)	3.90 ± 0.83	4.20	133 ± 31
[Mg VIII] (3.0276 μ m)	17.06 ± 1.54	18.33
(Narrow)	10.80 ± 1.53	11.60	170 ± 48
(Broad)	6.26 ± 0.10	6.73	378 ± 90
[Ca IV] (3.2061 μ m)	1.54 ± 0.55	1.66	142 ± 28
[Al VI] (3.6593 μ m)	1.90 ± 0.31	2.05	281 ± 74
[Si IX] (3.9357 μ m)	9.77 ± 0.50	11.52
(Narrow)	8.82 ± 0.25	9.49	102 ± 28
(Broad)	0.95 ± 0.25	1.03	466 ± 106
[Ca VII] (4.0864 μ m)	0.58 ± 0.27	0.70	186 ± 129
[Ca V] (4.1574 μ m)	2.20 ± 0.26	2.37	143 ± 28
[Mg IV] (4.4871 μ m)	12.70 ± 6.40	13.70	97 ± 22
[Ar VI] (4.5280 μ m)	45.90 ± 11.0	49.46
(Narrow)	43.80 ± 10.4	47.20	106 ± 23
(Broad)	2.10 ± 0.60	2.26	414 ± 72
[Na VII] (4.6834 μ m)	0.83 ± 0.28	0.89	136 ± 34

NOTE—Same as Table 7, but for J1009.

REFERENCES

- Allen, M. G., Groves, B. A., Dopita, M. A., Sutherland, R. S., & Kewley, L. J. 2008, *ApJS*, 178, 20, doi: [10.1086/589652](https://doi.org/10.1086/589652)
- Aravindan, A., Canalizo, G., Secrest, N., Satyapal, S., & Bohn, T. 2024, *ApJ*, 975, 60, doi: [10.3847/1538-4357/ad702b](https://doi.org/10.3847/1538-4357/ad702b)
- Aravindan, A., Liu, W., Canalizo, G., et al. 2023, *ApJ*, 950, 33, doi: [10.3847/1538-4357/acca7c](https://doi.org/10.3847/1538-4357/acca7c)
- Arjona-Gálvez, E., Di Cintio, A., & Grand, R. J. J. 2024, *A&A*, 690, A286, doi: [10.1051/0004-6361/202449439](https://doi.org/10.1051/0004-6361/202449439)
- Armus, L., Lai, T., U, V., et al. 2023, *ApJL*, 942, L37, doi: [10.3847/2041-8213/acac66](https://doi.org/10.3847/2041-8213/acac66)
- Asplund, M., Grevesse, N., Sauval, A. J., & Scott, P. 2009, *ARA&A*, 47, 481, doi: [10.1146/annurev.astro.46.060407.145222](https://doi.org/10.1146/annurev.astro.46.060407.145222)
- Astropy Collaboration, Robitaille, T. P., Tollerud, E. J., et al. 2013, *A&A*, 558, A33, doi: [10.1051/0004-6361/201322068](https://doi.org/10.1051/0004-6361/201322068)
- Astropy Collaboration, Price-Whelan, A. M., Sipőcz, B. M., et al. 2018, *AJ*, 156, 123, doi: [10.3847/1538-3881/aabc4f](https://doi.org/10.3847/1538-3881/aabc4f)
- Astropy Collaboration, Price-Whelan, A. M., Lim, P. L., et al. 2022, *ApJ*, 935, 167, doi: [10.3847/1538-4357/ac7c74](https://doi.org/10.3847/1538-4357/ac7c74)
- Atek, H., Labbé, I., Furtak, L. J., et al. 2024, *Nature*, 626, 975, doi: [10.1038/s41586-024-07043-6](https://doi.org/10.1038/s41586-024-07043-6)
- Baldassare, V. F., Reines, A. E., Gallo, E., & Greene, J. E. 2017, *ApJ*, 836, 20, doi: [10.3847/1538-4357/836/1/20](https://doi.org/10.3847/1538-4357/836/1/20)
- Baldwin, J. A., Phillips, M. M., & Terlevich, R. 1981, *PASP*, 93, 5, doi: [10.1086/130766](https://doi.org/10.1086/130766)
- Baron, D., & Netzer, H. 2019, *MNRAS*, 486, 4290, doi: [10.1093/mnras/stz1070](https://doi.org/10.1093/mnras/stz1070)
- Bianchin, M., U, V., Song, Y., et al. 2024, *ApJ*, 965, 103, doi: [10.3847/1538-4357/ad2a50](https://doi.org/10.3847/1538-4357/ad2a50)
- Blanton, M. R., Kazin, E., Muna, D., Weaver, B. A., & Price-Whelan, A. 2011, *AJ*, 142, 31, doi: [10.1088/0004-6256/142/1/31](https://doi.org/10.1088/0004-6256/142/1/31)
- Bohn, T., Canalizo, G., Satyapal, S., & Sales, L. V. 2022, *ApJ*, 931, 69, doi: [10.3847/1538-4357/ac6870](https://doi.org/10.3847/1538-4357/ac6870)
- Bohn, T., Canalizo, G., Veilleux, S., & Liu, W. 2021, *ApJ*, 911, 70, doi: [10.3847/1538-4357/abe70c](https://doi.org/10.3847/1538-4357/abe70c)
- Böker, T., Beck, T. L., Birkmann, S. M., et al. 2023, *PASP*, 135, 038001, doi: [10.1088/1538-3873/acb846](https://doi.org/10.1088/1538-3873/acb846)
- Brinchmann, J. 2023, *MNRAS*, 525, 2087, doi: [10.1093/mnras/stad1704](https://doi.org/10.1093/mnras/stad1704)
- Bushouse, H., Eisenhamer, J., Dencheva, N., et al. 2023,, 1.9.4 Zenodo, doi: [10.5281/zenodo.7577320](https://doi.org/10.5281/zenodo.7577320)
- Cai, W., Zhao, Y., Zhang, H.-X., Bai, J.-M., & Liu, H.-T. 2020, *ApJ*, 903, 58, doi: [10.3847/1538-4357/abb81c](https://doi.org/10.3847/1538-4357/abb81c)
- Cann, J. M., Satyapal, S., Abel, N. P., et al. 2019, *ApJL*, 870, L2, doi: [10.3847/2041-8213/aaf88d](https://doi.org/10.3847/2041-8213/aaf88d)
- Cann, J. M., Satyapal, S., Abel, N. P., et al. 2018, *ApJ*, 861, 142, doi: [10.3847/1538-4357/aac64a](https://doi.org/10.3847/1538-4357/aac64a)
- Cann, J. M., Satyapal, S., Rothberg, B., et al. 2021, *ApJL*, 912, L2, doi: [10.3847/2041-8213/abf56d](https://doi.org/10.3847/2041-8213/abf56d)
- Cappellari, M., & Emsellem, E. 2004, *PASP*, 116, 138, doi: [10.1086/381875](https://doi.org/10.1086/381875)
- Chadayammuri, U., Bogdán, Á., Ricarte, A., & Natarajan, P. 2023, *ApJ*, 946, 51, doi: [10.3847/1538-4357/acbea6](https://doi.org/10.3847/1538-4357/acbea6)
- Chilingarian, I. V., Katkov, I. Y., Zolotukhin, I. Y., et al. 2018, *ApJ*, 863, 1, doi: [10.3847/1538-4357/aad184](https://doi.org/10.3847/1538-4357/aad184)
- Chisholm, J., Berg, D. A., Endsley, R., et al. 2024, *MNRAS*, 534, 2633, doi: [10.1093/mnras/stae2199](https://doi.org/10.1093/mnras/stae2199)
- Clark, P., Graur, O., Callow, J., et al. 2024, *MNRAS*, 528, 7076, doi: [10.1093/mnras/stae460](https://doi.org/10.1093/mnras/stae460)
- Concas, A., Popesso, P., Brusa, M., et al. 2017, *A&A*, 606, A36, doi: [10.1051/0004-6361/201629519](https://doi.org/10.1051/0004-6361/201629519)
- Davies, R., Baron, D., Shimizu, T., et al. 2020, *MNRAS*, 498, 4150, doi: [10.1093/mnras/staa2413](https://doi.org/10.1093/mnras/staa2413)
- de Blok, W. J. G. 2010, *Advances in Astronomy*, 2010, 789293, doi: [10.1155/2010/789293](https://doi.org/10.1155/2010/789293)
- Del Zanna, G., Dere, K. P., Young, P. R., & Landi, E. 2021, *ApJ*, 909, 38, doi: [10.3847/1538-4357/abd8ce](https://doi.org/10.3847/1538-4357/abd8ce)
- Dere, K. P., Landi, E., Mason, H. E., Monsignori Fossi, B. C., & Young, P. R. 1997, *A&AS*, 125, 149, doi: [10.1051/aas:1997368](https://doi.org/10.1051/aas:1997368)
- Diaz-Santos, T., Lai, T. S. Y., Finnerty, L., et al. 2025,, Astrophysics Source Code Library, record ascl:2501.001 <http://ascl.net/2501.001>
- Dopita, M. A., & Sutherland, R. S. 1995, *ApJ*, 455, 468, doi: [10.1086/176596](https://doi.org/10.1086/176596)
- Evans, I. N. 1988, *ApJS*, 67, 373, doi: [10.1086/191276](https://doi.org/10.1086/191276)
- Ferguson, J. W., Korista, K. T., Baldwin, J. A., & Ferland, G. J. 1997, *ApJ*, 487, 122, doi: [10.1086/304611](https://doi.org/10.1086/304611)
- Filippenko, A. V., & Ho, L. C. 2003, *ApJL*, 588, L13, doi: [10.1086/375361](https://doi.org/10.1086/375361)
- Fonseca-Faria, M. A., Rodríguez-Ardila, A., Contini, M., Dahmer-Hahn, L. G., & Morganti, R. 2023, *MNRAS*, 524, 143, doi: [10.1093/mnras/stad1871](https://doi.org/10.1093/mnras/stad1871)
- Furtak, L. J., Zitrin, A., Plat, A., et al. 2023, *ApJ*, 952, 142, doi: [10.3847/1538-4357/acdc9d](https://doi.org/10.3847/1538-4357/acdc9d)
- Gelbord, J. M., Mullaney, J. R., & Ward, M. J. 2009, *MNRAS*, 397, 172, doi: [10.1111/j.1365-2966.2009.14961.x](https://doi.org/10.1111/j.1365-2966.2009.14961.x)
- Groves, B. A., & Allen, M. G. 2010, *NewA*, 15, 614, doi: [10.1016/j.newast.2010.02.005](https://doi.org/10.1016/j.newast.2010.02.005)
- Groves, B. A., Dopita, M. A., & Sutherland, R. S. 2004a, *ApJS*, 153, 75, doi: [10.1086/421114](https://doi.org/10.1086/421114)
- Groves, B. A., Dopita, M. A., & Sutherland, R. S. 2004b, *ApJS*, 153, 9, doi: [10.1086/421113](https://doi.org/10.1086/421113)

- Harikane, Y., Zhang, Y., Nakajima, K., et al. 2023, *ApJ*, 959, 39, doi: [10.3847/1538-4357/ad029e](https://doi.org/10.3847/1538-4357/ad029e)
- Hinkle, J. T., Tucker, M. A., Shappee, B. J., et al. 2023, *MNRAS*, 519, 2035, doi: [10.1093/mnras/stac3659](https://doi.org/10.1093/mnras/stac3659)
- Ho, L. C. 2005, *ApJ*, 629, 680, doi: [10.1086/431643](https://doi.org/10.1086/431643)
- Hutchison, T. A., Welch, B. D., Rigby, J. R., et al. 2024, *PASP*, 136, 044503, doi: [10.1088/1538-3873/ad34fd](https://doi.org/10.1088/1538-3873/ad34fd)
- Inayoshi, K., Visbal, E., & Haiman, Z. 2020, *ARA&A*, 58, 27, doi: [10.1146/annurev-astro-120419-014455](https://doi.org/10.1146/annurev-astro-120419-014455)
- Ishibashi, W., & Courvoisier, T. J. L. 2010, *A&A*, 512, A58, doi: [10.1051/0004-6361/200913587](https://doi.org/10.1051/0004-6361/200913587)
- Jakobsen, P., Ferruit, P., Alves de Oliveira, C., et al. 2022, *A&A*, 661, A80, doi: [10.1051/0004-6361/202142663](https://doi.org/10.1051/0004-6361/202142663)
- Kocevski, D. D., Onoue, M., Inayoshi, K., et al. 2023, *ApJL*, 954, L4, doi: [10.3847/2041-8213/ace5a0](https://doi.org/10.3847/2041-8213/ace5a0)
- Koudmani, S., Henden, N. A., & Sijacki, D. 2021, *MNRAS*, 503, 3568, doi: [10.1093/mnras/stab677](https://doi.org/10.1093/mnras/stab677)
- Koudmani, S., Sijacki, D., & Smith, M. C. 2022, *MNRAS*, 516, 2112, doi: [10.1093/mnras/stac2252](https://doi.org/10.1093/mnras/stac2252)
- Labbé, I., van Dokkum, P., Nelson, E., et al. 2023, *Nature*, 616, 266, doi: [10.1038/s41586-023-05786-2](https://doi.org/10.1038/s41586-023-05786-2)
- Lamperti, I., Koss, M., Trakhtenbrot, B., et al. 2017, *MNRAS*, 467, 540, doi: [10.1093/mnras/stx055](https://doi.org/10.1093/mnras/stx055)
- Law, D. R., Hawcroft, C., Smith, L. J., et al. 2024, *ApJL*, 976, L25, doi: [10.3847/2041-8213/ad91a6](https://doi.org/10.3847/2041-8213/ad91a6)
- Liu, G., Zakamska, N. L., Greene, J. E., Nesvadba, N. P. H., & Liu, X. 2013, *MNRAS*, 436, 2576, doi: [10.1093/mnras/stt1755](https://doi.org/10.1093/mnras/stt1755)
- Liu, W., Veilleux, S., Canalizo, G., et al. 2020, *ApJ*, 905, 166, doi: [10.3847/1538-4357/abc269](https://doi.org/10.3847/1538-4357/abc269)
- Liu, W., Veilleux, S., Canalizo, G., et al. 2024, *ApJ*, 965, 152, doi: [10.3847/1538-4357/ad2b63](https://doi.org/10.3847/1538-4357/ad2b63)
- Luridiana, V., Morisset, C., & Shaw, R. A. 2015, *A&A*, 573, A42, doi: [10.1051/0004-6361/201323152](https://doi.org/10.1051/0004-6361/201323152)
- Maiolino, R., Scholtz, J., Witstok, J., et al. 2024, *Nature*, 627, 59, doi: [10.1038/s41586-024-07052-5](https://doi.org/10.1038/s41586-024-07052-5)
- Manzano-King, C. M., Canalizo, G., & Sales, L. V. 2019, *ApJ*, 884, 54, doi: [10.3847/1538-4357/ab4197](https://doi.org/10.3847/1538-4357/ab4197)
- Marleau, F. R., Clancy, D., Habas, R., & Bianconi, M. 2017, *A&A*, 602, A28, doi: [10.1051/0004-6361/201629832](https://doi.org/10.1051/0004-6361/201629832)
- Matzko, W., Satyapal, S., Reece, M., et al. 2025, *ApJ*, 984, 170, doi: [10.3847/1538-4357/adc92f](https://doi.org/10.3847/1538-4357/adc92f)
- May, D., Rodríguez-Ardila, A., Prieto, M. A., et al. 2018, *MNRAS*, 481, L105, doi: [10.1093/mnrasl/sly155](https://doi.org/10.1093/mnrasl/sly155)
- Mazzalay, X., Rodríguez-Ardila, A., & Komossa, S. 2010, *MNRAS*, 405, 1315, doi: [10.1111/j.1365-2966.2010.16533.x](https://doi.org/10.1111/j.1365-2966.2010.16533.x)
- Mazzalay, X., Rodríguez-Ardila, A., Komossa, S., & McGregor, P. J. 2013, *MNRAS*, 430, 2411, doi: [10.1093/mnras/stt064](https://doi.org/10.1093/mnras/stt064)
- McKaig, J. D., Satyapal, S., Laor, A., et al. 2024, *ApJ*, 976, 130, doi: [10.3847/1538-4357/ad7a79](https://doi.org/10.3847/1538-4357/ad7a79)
- Mezcua, M., & Domínguez Sánchez, H. 2020, *ApJL*, 898, L30, doi: [10.3847/2041-8213/aba199](https://doi.org/10.3847/2041-8213/aba199)
- Molina, M., Reines, A. E., Latimer, L. J., Baldassare, V., & Salehirad, S. 2021, *ApJ*, 922, 155, doi: [10.3847/1538-4357/ac1ffa](https://doi.org/10.3847/1538-4357/ac1ffa)
- Moran, E. C., Shahinyan, K., Sugarman, H. R., Vélez, D. O., & Eracleous, M. 2014, *AJ*, 148, 136, doi: [10.1088/0004-6256/148/6/136](https://doi.org/10.1088/0004-6256/148/6/136)
- Müller-Sánchez, F., Prieto, M. A., Hicks, E. K. S., et al. 2011, *ApJ*, 739, 69, doi: [10.1088/0004-637X/739/2/69](https://doi.org/10.1088/0004-637X/739/2/69)
- Murayama, T., & Taniguchi, Y. 1998, *ApJL*, 497, L9, doi: [10.1086/311264](https://doi.org/10.1086/311264)
- Nagao, T., Murayama, T., Shioya, Y., & Taniguchi, Y. 2003, *AJ*, 125, 1729, doi: [10.1086/368248](https://doi.org/10.1086/368248)
- Nagao, T., Taniguchi, Y., & Murayama, T. 2000, *AJ*, 119, 2605, doi: [10.1086/301411](https://doi.org/10.1086/301411)
- Negus, J., Comerford, J. M., Müller Sánchez, F., et al. 2021, *ApJ*, 920, 62, doi: [10.3847/1538-4357/ac1343](https://doi.org/10.3847/1538-4357/ac1343)
- Negus, J., Comerford, J. M., Sánchez, F. M., et al. 2023, *ApJ*, 945, 127, doi: [10.3847/1538-4357/acb772](https://doi.org/10.3847/1538-4357/acb772)
- Osterbrock, D. E., & Ferland, G. J. 2006, *Astrophysics of gaseous nebulae and active galactic nuclei*
- Pelat, D., Alloin, D., & Fosbury, R. A. E. 1981, *MNRAS*, 195, 787, doi: [10.1093/mnras/195.4.787](https://doi.org/10.1093/mnras/195.4.787)
- Penny, S. J., Masters, K. L., Smethurst, R., et al. 2018, *MNRAS*, 476, 979, doi: [10.1093/mnras/sty202](https://doi.org/10.1093/mnras/sty202)
- Penston, M. V., Fosbury, R. A. E., Boksenberg, A., Ward, M. J., & Wilson, A. S. 1984, *MNRAS*, 208, 347, doi: [10.1093/mnras/208.2.347](https://doi.org/10.1093/mnras/208.2.347)
- Perna, M., Arribas, S., Marshall, M., et al. 2023, *A&A*, 679, A89, doi: [10.1051/0004-6361/202346649](https://doi.org/10.1051/0004-6361/202346649)
- Piconcelli, E., Jimenez-Bailón, E., Guainazzi, M., et al. 2005, *A&A*, 432, 15, doi: [10.1051/0004-6361:20041621](https://doi.org/10.1051/0004-6361:20041621)
- Prieto, A., Rodríguez-Ardila, A., Panda, S., & Marinello, M. 2022, *MNRAS*, 510, 1010, doi: [10.1093/mnras/stab3414](https://doi.org/10.1093/mnras/stab3414)
- Prieto, M. A., Marco, O., & Gallimore, J. 2005, *MNRAS*, 364, L28, doi: [10.1111/j.1745-3933.2005.00099.x](https://doi.org/10.1111/j.1745-3933.2005.00099.x)
- Pucha, R., Juneau, S., Dey, A., et al. 2025, *ApJ*, 982, 10, doi: [10.3847/1538-4357/adb1dd](https://doi.org/10.3847/1538-4357/adb1dd)
- Reece, M., Satyapal, S., Sexton, R. O., et al. 2022, *ApJ*, 936, 140, doi: [10.3847/1538-4357/ac8981](https://doi.org/10.3847/1538-4357/ac8981)
- Reece, M., Satyapal, S., Sexton, R. O., et al. 2023, *ApJL*, 946, L38, doi: [10.3847/2041-8213/acb4e4](https://doi.org/10.3847/2041-8213/acb4e4)
- Reines, A. E., Greene, J. E., & Geha, M. 2013, *ApJ*, 775, 116, doi: [10.1088/0004-637X/775/2/116](https://doi.org/10.1088/0004-637X/775/2/116)
- Reines, A. E., & Volonteri, M. 2015, *ApJ*, 813, 82, doi: [10.1088/0004-637X/813/2/82](https://doi.org/10.1088/0004-637X/813/2/82)

- Richardson, C. T., Simpson, C., Polimera, M. S., et al. 2022, *ApJ*, 927, 165, doi: [10.3847/1538-4357/ac510c](https://doi.org/10.3847/1538-4357/ac510c)
- Riffel, R., Rodríguez-Ardila, A., & Pastoriza, M. G. 2006, *A&A*, 457, 61, doi: [10.1051/0004-6361:20065291](https://doi.org/10.1051/0004-6361:20065291)
- Rodríguez-Ardila, A., & Fonseca-Faria, M. A. 2020, *ApJL*, 895, L9, doi: [10.3847/2041-8213/ab901b](https://doi.org/10.3847/2041-8213/ab901b)
- Rodríguez-Ardila, A., Fonseca-Faria, M. A., Dahmer-Hahn, L. G., et al. 2025, *MNRAS*, 538, 2800, doi: [10.1093/mnras/staf430](https://doi.org/10.1093/mnras/staf430)
- Rodríguez-Ardila, A., Prieto, M. A., Mazzalay, X., et al. 2017, *MNRAS*, 470, 2845, doi: [10.1093/mnras/stx1401](https://doi.org/10.1093/mnras/stx1401)
- Rodríguez-Ardila, A., Prieto, M. A., Portilla, J. G., & Tejeiro, J. M. 2011, *ApJ*, 743, 100, doi: [10.1088/0004-637X/743/2/100](https://doi.org/10.1088/0004-637X/743/2/100)
- Rodríguez-Ardila, A., Prieto, M. A., Viegas, S., & Gruenwald, R. 2006, *ApJ*, 653, 1098, doi: [10.1086/508864](https://doi.org/10.1086/508864)
- Rodríguez-Ardila, A., Viegas, S. M., Pastoriza, M. G., & Prato, L. 2002, *ApJ*, 579, 214, doi: [10.1086/342840](https://doi.org/10.1086/342840)
- Rodríguez Morales, V., Mezcuca, M., Domínguez Sánchez, H., et al. 2025, *A&A*, 697, A235, doi: [10.1051/0004-6361/202453481](https://doi.org/10.1051/0004-6361/202453481)
- Salehirad, S., Reines, A. E., & Molina, M. 2022, *ApJ*, 937, 7, doi: [10.3847/1538-4357/ac8876](https://doi.org/10.3847/1538-4357/ac8876)
- Salehirad, S., Reines, A. E., & Molina, M. 2025, *ApJ*, 979, 26, doi: [10.3847/1538-4357/ad9a57](https://doi.org/10.3847/1538-4357/ad9a57)
- Satyapal, S., Kamal, L., Cann, J. M., Secrest, N. J., & Abel, N. P. 2021, *ApJ*, 906, 35, doi: [10.3847/1538-4357/abfbaf](https://doi.org/10.3847/1538-4357/abfbaf)
- Scholtz, J., Harrison, C. M., Rosario, D. J., et al. 2021, *MNRAS*, 505, 5469, doi: [10.1093/mnras/stab1631](https://doi.org/10.1093/mnras/stab1631)
- Sexton, R. O., Matzko, W., Darden, N., Canalizo, G., & Gorjian, V. 2021, *MNRAS*, 500, 2871, doi: [10.1093/mnras/staa3278](https://doi.org/10.1093/mnras/staa3278)
- Silk, J. 2011, in *IAU Symposium*, Vol. 277, Tracing the Ancestry of Galaxies, ed. C. Carignan, F. Combes, & K. C. Freeman, 273–281, doi: [10.1017/S1743921311022939](https://doi.org/10.1017/S1743921311022939)
- Silk, J. 2017, *ApJL*, 839, L13, doi: [10.3847/2041-8213/aa67da](https://doi.org/10.3847/2041-8213/aa67da)
- U, V., Medling, A., Sanders, D., et al. 2013, *ApJ*, 775, 115, doi: [10.1088/0004-637X/775/2/115](https://doi.org/10.1088/0004-637X/775/2/115)
- U, V., Lai, T., Bianchin, M., et al. 2022, *ApJL*, 940, L5, doi: [10.3847/2041-8213/ac961c](https://doi.org/10.3847/2041-8213/ac961c)
- Vazdekis, A., Koleva, M., Ricciardelli, E., Röck, B., & Falcón-Barroso, J. 2016, *MNRAS*, 463, 3409, doi: [10.1093/mnras/stw2231](https://doi.org/10.1093/mnras/stw2231)
- Veilleux, S., Maiolino, R., Bolatto, A. D., & Aalto, S. 2020, *A&A Rv*, 28, 2, doi: [10.1007/s00159-019-0121-9](https://doi.org/10.1007/s00159-019-0121-9)
- Volonteri, M., Habouzit, M., & Colpi, M. 2021, *Nature Reviews Physics*, 3, 732, doi: [10.1038/s42254-021-00364-9](https://doi.org/10.1038/s42254-021-00364-9)
- Yang, C.-W., Wang, T.-G., Ferland, G., et al. 2013, *ApJ*, 774, 46, doi: [10.1088/0004-637X/774/1/46](https://doi.org/10.1088/0004-637X/774/1/46)
- Yang, J., Gurvits, L. I., Paragi, Z., et al. 2020, *MNRAS*, 495, L71, doi: [10.1093/mnrasl/slaa052](https://doi.org/10.1093/mnrasl/slaa052)